POLITECNICO
DI TORINO

Corso di Laurea Magistrale in Ingegneria Aerospaziale

Tesi di Laurea Magistrale

External Aerodynamics Optimisation using the Adjoint Method

Supervisore Aziendale
Ing. Laura Maria Lorefice

Relatore
Ing. Domenic D'Ambrosio

Corelatore
Prof. Gaetano Iuso

Candidato
Gianluca Francesconi

Marzo 2018

Sommario

Questa tesi, svolta presso il dipartimento Aerothermal di FCA ad Orbassano, si propone di studiare le potenzialità del solutore Adjoint implementato in STAR-CCM+ applicandolo ad un problema di ottimizzazione dell'aerodinamica esterna. Nel caso in esame l'obiettivo è ridurre la resistenza aerodinamica della Fiat Tipo 5 porte. Il metodo Adjoint consente di studiare l'influenza di un certo numero di parametri di progetto, in questo caso le forme della vettura, su una determinata funzione obiettivo da minimizzare o massimizzare, indirizzando le modifiche della geometria al raggiungimento di una configurazione ottimale.

Sono state seguite due diverse procedure di ottimizzazione, utilizzando gli strumenti di morphing forniti dal software CFD STAR-CCM+ e dal software CAE ANSA Pre-processor, al fine di determinare quale potesse garantire risultati migliori in termini di qualità e di costo computazionale ed eventualmente essere implementata in un processo automatizzato.

Le simulazioni fluidodinamiche alla base dell'analisi di ottimizzazione sono condotte utilizzando i modelli di turbolenza k-ε e k-ω associati alle RANS, attualmente le sole equazioni con cui il solutore Adjoint fornito può essere eseguito. Una simulazione stazionaria per l'aerodinamica esterna rappresenta un compromesso tra il costo computazionale e l'accuratezza dei risultati. In tutte le casistiche analizzate si è riusciti a ridurre la resistenza aerodinamica del veicolo di circa il 4% tramite modifiche di dettaglio, essendo il modello in produzione già vicino alla configurazione ottima.

Il metodo Adjoint ha però evidenziato diversi limiti. Una discretizzazione al primo ordine delle equazioni aggiunte, a fronte del secondo ordine impiegato per le equazioni fluidodinamiche, è stata utilizzata per garantire la convergenza, preferendo una maggiore robustezza a scapito dell'accuratezza. Questo si è reso necessario a causa della complessità del problema di natura industriale. Futuri studi potrebbero prevedere di eseguire simulazioni al secondo ordine su modelli semplificati per valutare eventuali differenze con il primo ordine nella soluzione. Elevati tempi di calcolo abbinati alle simulazioni condotte con il modello k-ω, associati ad un'estrema sensibilità del solutore alle imperfezioni della mesh, rendono al momento questo modello incompatibile con le tempistiche dei processi di sviluppo. Una ricerca sul setup più adatto alla k-ω potrebbe consentire di sfruttare la maggior accuratezza del modello di turbolenza per i casi di aerodinamica esterna, in attesa di riuscire ad eseguire l'Adjoint anche su simulazioni DES.

Contents

List of Figures

List of Tables

Chapter 1

Introduction

1.1 Background

Nowadays, Computational Fluid Dynamics (CFD) is an essential tool across automotive industries for the assessment and the optimisation of vehicle resistance in the design phase. It is applied not only for vehicle external aerodynamics, but also for ducted flows, cooling and ventilation, internal combustion engines, aero-acoustics and many other applications.

One of the main objectives of the aerodynamic design is the reduction of the drag, in order to maintain fuel consumption and pollution emissions as low as possible. This scope can be pursued in two ways: using the so called "aerodynamic add-on" and with the research of a suitable external shape. However, the former is constrained by costs and industrial development processes and the latter is subjected to aesthetic considerations and ergonomics, limiting the design exploration space.

The standard design procedure consists in a collaboration between designers and aerodynamicists, with an iterative trade off between different modified configurations to find the best compromise. Thanks to CFD it is possible to evaluate several aspects in the early stage design; moreover there is no need to build several models for wind tunnel testing, reducing development costs. However, wind tunnel is still used for fine tuning purposes and to confirm the performance of the final configuration before road test.

Traditional approaches to CFD optimisations involve the generation of a DOE (Design of Experiments) and the application of different optimisation algorithms, requires a lot of time and a great effort of computational resources for the evaluation of the influence of many design parameters involved in the optimisation loop.

For these reasons gradient-based methods have been developed for aerodynamic optimisation, and the adjoint method is among them. Its main advantage is that the computational cost is independent from the number of design variables, allowing to explore a

potential infinite number of geometrical parameters performing only a primal flow solution and a single adjoint solution.

The adjoint method has been studied since 70's by Pironneau, who solved the adjoint system for design purposes [1]. Jameson was the first to study the adjoint in aeronautical field, developing also a complete formulation for Navier-Stokes equations [2]. In automotive industry it has been introduced especially during the last decade, thanks to the increasing contribution and power of CFD. Many papers on the topic explore the possibility to use adjoint method for external aerodynamics. Othmer for Volkswagen Group proposes applications on RANS (Reynolds Averaged Navier-Stokes) and DES (Detached Eddy Simulation) turbulence models [3].

There are two different approaches: discrete adjoint and continuous adjoint. In the former the partial differential equations are discretized before the adjoint differentiation, while in the latter the adjoint equations are formulated by differentiating the governing PDEs. Then adjoint equations are discretized and solved [4]. There are several differences between these two approaches, in particular respect to the complexity of implementation and the computational cost; see references [5] and [6] for details.

The adjoint method allows to predict the influence of the design parameters - i.e. mesh nodes displacement - on an objective function that must be minimised or maximised; in this case the drag of the car must be reduced. The computation of surface sensitivity gives indications on critical areas where it is convenient to change the geometry. One of the main issues in the application of adjoint methods on actual automotive problems is due to the complexity of the geometries, indeed the adjoint equation system is influenced by the quality of the computational mesh, that requires a high quality in order to reach an adequate level of convergence.

1.2 Scope

This work, carried on at FCA Aerothermal PCC Department in Orbassano, has the aim to verify the possibility to implement the adjoint method into the design process and determine what is the most efficient procedure for an aerodynamic optimisation in terms of accuracy, robustness and computation time, using different tools. An application is performed on Fiat Tipo 5 Porte (Hatchback), showed in Figure 1.

From a solver point of view it has been decided to test the adjoint solver and the optimisation process of the commercial code STAR-CCM+®. This solver has been developed throughout the years and now it permits to compute surface sensitivity and mesh sensitivity of the cost function with regard to position of some control points or physical quantities in the flow field and to perform mesh deformation.

To achieve our scope two different methodologies are followed, performing the shape optimisation using both the capabilities of the CFD software and the morphing tool of Beta CAE ANSA Pre-processor. A first simulation to visualize the results in terms of drag and drag coefficient C_D is performed. All the results are defined as a percentage of the first C_D. Then a run with the adjoint solver provides the sensitivity of the objective function. We focus our attention on parts with the major contribution on drag and on others that are essential to control flow separation, positioning control points where the mesh sensitivity is computed. STAR-CCM+ morphing tool will be used to deform mesh iteratively with a first-order steepest descent algorithm until a satisfactory result is reached, without losing volume mesh quality.

Considering the possibility to employ an external optimisation tool, after the primal simulation results in terms of surface sensitivity maps are imported into ANSA to perform direct morphing of the critical areas of the model. The modified geometry is imported again in STAR-CCM+ to run a primal simulation and verify the reduction of the aerodynamic drag.

Figure 1.1. Fiat Tipo 5 Porte.

Chapter 2

Theory

In this chapter there is an overview on Navier-Stokes equations and RANS equations in order to explain the physics setup of the simulations performed in this work. As RANS equations form an unclosed system, the Boussinesq hypothesis is introduced to model the unknown Reynolds stress tensor. A brief presentation of two of the most famous and reliable turbulence models used in industrial application is proposed. For any details about modelling turbulence and the models showed in this chapter, see references [7] and [8].

2.1 Navier-Stokes equations

Fluid Dynamics is governed by three fundamental physical laws: the conservation of mass, momentum and energy. The Navier-Stokes equations, coupled with boundary conditions, represent the mathematical model of these physical principles and they come from a model of flow, that can be in the Eulerian or Lagrangian approach, depending respectively on the choice of a control volume fixed in space or moving with the observed fluid particles. In the first approach the equations are expressed in conservation or divergence form, in the latter the mathematical form is defined as non-conservative. Equations can be in differential form, if the control volume is infinitesimally small, or in integral form if the control volume is a finite region of the fluid. All these forms can be obtained with some manipulation one from the other.

As Navier-Stokes equations can not be solved exactly, in Computational Fluid Dynamics they are discretised to be converted from a closed-form, where the functions have an infinite continuum of values throughout the entire domain, into a set of algebraic equations where the values of the functions are known only at a finite number of discrete points in the domain [9]. There are three discretisation methods: finite difference for differential equations, finite volume or finite element for integral equations.

For an unsteady incompressible flow the continuity equation and the momentum equations in differential conservation form, written with the Einstein notation, are

$$\frac{\partial U_i}{\partial x_i} = 0 \tag{2.1}$$

$$\rho\left[\frac{\partial U_i}{\partial t} + \frac{\partial}{\partial x_j}(U_i U_j)\right] = -\frac{\partial p}{\partial x_i} + \mu\frac{\partial}{\partial x_j}\left(\frac{\partial U_i}{\partial x_j} + \frac{\partial U_j}{\partial x_i}\right) \tag{2.2}$$

As the continuity equation is independent from the time, it represents a kinematic constraint that must be satisfied by the momentum equations. When the flow is incompressible, temperature variations are negligible and the energy equation is uncoupled from the others. In this case, where only the external aerodynamics has to be studied and so any kind of thermal exchange is excluded, the energy equation is not solved, thus for the sake of simplicity it is not introduced.

As STAR-CCM+ discretises the Navier-Stokes equations using the Finite Volume Method, we have to write them in integral conservation form as follows

$$\int_S \rho\mathbf{U}\cdot\mathbf{n}dS = 0 \tag{2.3}$$

$$\int_V \frac{\partial(\rho\mathbf{U})}{\partial t}dV + \int_S \rho\mathbf{U}(\mathbf{U}\cdot\mathbf{n})dS = -\int_S p\mathbf{n}dS + \int_S \tau\cdot\mathbf{n}dS \tag{2.4}$$

The term τ in the last integral in the momentum equation represents the viscous stress tensor and it is related to the velocity gradients. For incompressible flows its expression is the same shown in the last term of equation (2.2), where the divergence comes from the Gauss theorem applied to the surface integral.

2.1.1 Finite Volume Discretisation

In the finite volume discretisation the fluid domain is divided into a finite number of control volumes, defined as cells, where the solution is known at the centroid of each cell. This discrete representation of the domain is defined as numerical or computational grid, or more simply mesh. For finite volume methods the grid is generally unstructured, resulting in a more complex matrix of the equation system. The conservation laws have to be fulfilled locally for each control volume and globally in the entire domain. Volume and surface integrals have to be approximated in some manner to be discretised. Surface integrals, that represent convective and diffusive fluxes, are expressed in terms of known variable values at cell centres. For surface integrals the midpoint rule assumes that the flux has its mean value at the center of the cell face and it is multiplied for the face area.

Instead for volume integrals the discretisation is equal to the product of the mean value of the function at the cell centre and the cell volume. The numerical method chosen to solve the equation system has the property of consistency when the difference between the exact and the discretised equations, and thus the discretisation, tends to zero as the grid spacing tends to zero.

2.2 RANS

Though the Navier-Stokes equations describe completely all the aspects of turbulence, for industrial cases doing a direct numerical simulation (DNS) is quite impossible, because the computational cost and the number of mesh cells increase with the third power of the Reynolds number, that for a car is in the order of 10^6.

In most cases for external aerodynamics simulations knowing the mean flow field can be sufficient and solving the RANS (Reynolds Averaged Navier-Stokes) equations is a good compromise between the computational time and the accuracy of results. While turbulence is always unsteady and three-dimensional, mean flow field can be statistically steady. For a steady flow, the mean is simply a time averaging process.

For the velocity field and all other physical quantities the Reynolds decomposition is applied, dividing each term into its mean and the fluctuation. To obtain the equations we consider a general unsteady flow, where velocity and pressure fields are respectively

$$\mathbf{U}(\mathbf{x},t) = \overline{\mathbf{U}}(\mathbf{x},t) + \mathbf{u}'(\mathbf{x},t) \tag{2.5}$$

$$p(\mathbf{x},t) = \overline{p}(\mathbf{x},t) + p'(\mathbf{x},t) \tag{2.6}$$

These expressions are substituted into the Navier-Stokes equations and then the mean of them is taken. Remembering that mean is a linear operator, and so it can be exchanged with derivatives, and that the mean of fluctuations is zero, the continuity equation for the mean velocity field maintains the same expression

$$\frac{\partial \overline{U}_i}{\partial x_i} = 0 \tag{2.7}$$

Taking the mean of the momentum equation is more complicated because of the convective term, that is non-linear. In fact we have the velocity covariances $\overline{U_i U_j}$, but we would have the product of mean velocities. The term is rewritten with respect to fluctuations using the Reynolds decomposition in this manner

$$\overline{U_i U_j} = \overline{(\overline{U_i} + u_i')(\overline{U_j} + u_j')} = \overline{\overline{U}_i \overline{U}_j + \overline{U}_i u_j' + \overline{U}_j u_i' + \overline{u'}_i \overline{u'}_j} = \overline{U}_i \overline{U}_j + \overline{u_i' u_j'} \tag{2.8}$$

Therefore substituting this expression into the divergence term on the left-hand side of (2.2) and reordering, the momentum equation in conservative form becomes

$$\rho\left[\frac{\partial \overline{U}_i}{\partial t} + \frac{\partial}{\partial x_j}(\overline{U}_i \overline{U}_j)\right] = -\frac{\partial \overline{p}}{\partial x_i} + \mu \frac{\partial}{\partial x_j}\left(\frac{\partial \overline{U}_i}{\partial x_j} + \frac{\partial \overline{U}_j}{\partial x_i}\right) - \frac{\partial}{\partial x_j}(\rho \overline{u_i' u_j'}) \tag{2.9}$$

The term $-\rho\overline{u_i' u_j'}$ is the Reynolds stress tensor. It is symmetric and therefore there are six independent terms. Physically it represents the momentum transfer due to the fluctuating velocity field. If the Reynolds stress tensor were equal to zero, RANS and Navier-Stokes equations would be identical, therefore it represents a crucial term in modelling turbulence [7].

Equations (2.7) and (2.9) form a system that is not closed, because in 3D problems there are four equations and ten unknowns: three velocities, the pressure and six Reynolds stresses. This is defined as the closure problem, so we need to find a way to write Reynolds stresses with respect to the mean flow quantities. This is possible only with a turbulence model.

2.3 Boussinesq hypothesis

Most turbulence models use the Boussinesq hypothesis, introduced in 1877, to model Reynolds stress tensor like a gradient-diffusion term. This hypothesis is based on the idea that eddies in turbulence behave with respect to the mean flow field as molecules behave with respect to the macroscopic motion. In fact as the diffusive terms in the Navier-Stokes equations describe the momentum transfer by molecular agitation so vortices transport momentum by fluctuations. For this reason the Reynolds stress tensor can be modelled with the same mathematical form of diffusive terms introducing a turbulent viscosity, or eddy viscosity, μ_T.

The Reynolds stress tensor, unlike the viscous stress tensor, has a non-zero trace that is proportional to the double of the turbulent kinetic energy k

$$-\rho\overline{u_i' u_i'} = -2\rho k \tag{2.10}$$

Therefore Reynolds stresses can be divided into an isotropic part, i.e. the trace, and an anisotropic one, simply by adding and subtracting the expression (2.10), obtaining

$$\tau_{ij}^{(R)} = -\frac{1}{3}\rho\overline{u_k' u_k'}\delta_{ij} - \rho\left(\overline{u_i' u_j'} - \frac{1}{3}\overline{u_k' u_k'}\delta_{ij}\right) \tag{2.11}$$

where δ_{ij} is the Kronecker delta and with the subscript k we refer to the summation over

repeated index. Only the anisotropic part is responsible for transporting momentum. Now the Boussinesq hypothesis gives the relation between fluctuations and the mean field: the assumption is that the anisotropic part of the Reynolds stress tensor, defined as a_{ij}, is determined by the mean velocity gradients

$$a_{ij} = 2\mu_T \overline{S}_{ij} = \mu_T \left(\frac{\partial \overline{U}_i}{\partial x_j} + \frac{\partial \overline{U}_j}{\partial x_i} \right) \tag{2.12}$$

where $\overline{S}_{ij}$ is the mean rate-of-strain tensor. Indeed assuming that a_{ij} and $\overline{S}_{ij}$ are aligned is a strong hypothesis, because this is not true even for most simple turbulent flows. However the Boussinesq hypothesis is accepted because it provides a convenient closure to the system. Reynolds stresses become

$$\tau_{ij}^{(R)} = -\frac{1}{3}\rho \overline{u'_k u'_k} \delta_{ij} + 2\mu_T \overline{S}_{ij} \tag{2.13}$$

Substituting them into the equation (2.9) and rearranging similar terms we obtain

$$\frac{\partial \overline{U}_i}{\partial t} + \frac{\partial}{\partial x_j}(\overline{U}_i \overline{U}_j) = -\frac{1}{\rho}\frac{\partial}{\partial x_i}\left(\overline{p} + \frac{2}{3}\rho k \right) + \frac{\partial}{\partial x_j}\left[(\nu + \nu_T)\left(\frac{\partial \overline{U}_i}{\partial x_j} + \frac{\partial \overline{U}_j}{\partial x_i} \right) \right] \tag{2.14}$$

The first thing which can be noted is that the term in the gradient on the right-hand side is a modified mean pressure. It accounts for the isotropic part of the Reynolds stress tensor, represented by the turbulent kinetic energy, and generally for an incompressible flow it is computed without separating two contributions. In fact the turbulent part of the modified pressure is often negligible with respect to the variations of the mean pressure. Equation (2.14) has the same form of (2.2), but the system is still not closed because there is another unknown, i.e. the turbulent viscosity ν_T and it must be modelled somehow. This is not easy, because the turbulent viscosity is not a property of the *fluid* like the kinematic viscosity ν, but it depends on the structure of fluctuations and thus it is a property of the *flow* and function of space and time. With dimensional considerations, the turbulent viscosity can be modelled as the product between a characteristic velocity and a characteristic length

$$\nu_T(\mathbf{x}, t) = velocity \cdot length \quad [m^2/s] \tag{2.15}$$

The algebraic models are based on this idea, for example the Prandtl's mixing-length model, that is the simplest one. Prandtl defined the turbulent viscosity as proportional

to the gradient of mean velocity in the following way

$$\nu_T = l_{mix}^2 \left| \frac{\partial \overline{U}}{\partial y} \right| \tag{2.16}$$

where l_{mix}, function of space, is the characteristic dimension of the biggest eddies. This model works well in the log-law layer of the boundary layer and for quasi-parallel flows, because the mixing-length is proportional to the wall distance, but it is poor for other turbulent flows, in which l_{mix} has to be determined with a guesswork and probably bad accuracy. Therefore the problem of determining the turbulent viscosity is only moved on determining l_{mix}.

2.4 Two-equation models

Knowing the value of the two characteristic quantities everywhere in the flow field is quite difficult, therefore other models were developed linking velocity and length to other quantities described by one or more transport equations. Spalart-Allmaras is the most known one-equation model, in which an empirical equation for the turbulent viscosity is written. Two of the most used two-equation models are k-ε and k-ω. Both these model have in common the transport equation for the turbulent kinetic energy k.

2.4.1 k-ε model

First Kolmogorov (1942) and then Prandtl (1945) suggested that the characteristic velocity v could be linked to the turbulent kinetic energy per unit mass k introduced in (2.10)

$$v = ck^{\frac{1}{2}} \tag{2.17}$$

where c is a constant. As the turbulent kinetic energy is a physical quantity, a model transport equation for it can be defined

$$\frac{\partial k}{\partial t} + \overline{U}_j \frac{\partial k}{\partial x_j} = P_k - \varepsilon + \frac{\partial I_j}{\partial x_j} \tag{2.18}$$

On the left-hand side there is the substantial derivative of k and on the right-hand side there are three general terms of production, dissipation and transport, defined as the flux of I_j. The production term represents the rate at which kinetic energy is transferred between mean flow and fluctuations and it is defined as

$$P_k = -\overline{u_i' u_j'} \frac{\partial \overline{U_i}}{\partial x_j} \tag{2.19}$$

The term ε is the dissipation per unit mass due to the molecular diffusion on the smallest scales of turbulence and it has the following expression

$$\varepsilon = \nu \overline{\frac{\partial u_i'}{\partial x_k} \frac{\partial u_i'}{\partial x_k}} \tag{2.20}$$

Finally I_j is modelled as

$$I_j = \nu \frac{\partial k}{\partial x_j} - \frac{1}{2} \overline{u_i' u_i' u_j'} - \frac{1}{\rho} \overline{p' u_j'} \tag{2.21}$$

where the first term is the molecular diffusion of the turbulent kinetic energy and the others represent the turbulent transport due to fluctuations and their correlation with pressure. The resultant equation is still exact, but the problem remains unclosed. In fact we have new unknowns in the turbulent transport term, i.e. the triple correlation and the correlation between fluctuations velocity and pressure. Therefore it is modelled with a gradient-diffusion hypothesis introducing the coefficient σ_k, that accounts for the different behaviour of all the eddies in turbulence. The model transport equation for the turbulent kinetic energy is rewritten as follows

$$\frac{\partial k}{\partial t} + \overline{U}_j \frac{\partial k}{\partial x_j} = -\overline{u_i' u_j'} \frac{\partial \overline{U}_i}{\partial x_j} - \varepsilon + \frac{\partial}{\partial x_j} \left[\left(\nu + \frac{\nu_T}{\sigma_k} \right) \frac{\partial k}{\partial x_j} \right] \tag{2.22}$$

This equation is the base for the most common turbulence models. Also the the dissipation remains unknown, because it is function of fluctuations. If we consider homogeneous isotropic turbulence, we can use Kolmogorov scales to find a relation between the turbulent length scale l and the turbulent energy. In fact Kolmogorov defines the rate of dissipation of turbulence energy ε as

$$\varepsilon \approx \frac{u'^3}{l} = \frac{k^{3/2}}{l} \tag{2.23}$$

Inverting this relation and remembering (2.17), the turbulent viscosity can be written as follows

$$\nu_T = C_\mu \frac{k^2}{\varepsilon} \tag{2.24}$$

At this point the second model equation for ε is introduced and it closes the system. In this manner, the length scale and the characteristic velocity can be obtained respectively from the dissipation and the turbulent kinetic energy to compute the eddy viscosity ν_T. The second model equation stems from empirical considerations. In fact, it is possible to write an exact equation considering ε as the responsible for the processes in the dissipation range, but it is more useful referring to it as the energy flow rate from the large eddies in the energy cascade, where ε is independent of the kinematic viscosity at high Reynolds

number. Therefore, without entering in any details, the model equation is the following

$$\frac{\partial \varepsilon}{\partial t} + \overline{U}_j \frac{\partial \varepsilon}{\partial x_j} = -C_{\varepsilon 1} \frac{\varepsilon}{k} \overline{u_i' u_j'} \frac{\partial \overline{U}_i}{\partial x_j} - C_{\varepsilon 2} \frac{\varepsilon^2}{k} + \frac{\partial}{\partial x_j} \left[\left(\nu + \frac{\nu_T}{\sigma_\varepsilon} \right) \frac{\partial \varepsilon}{\partial x_j} \right] \tag{2.25}$$

Thus there are five closure coefficients, whose values, also implemented in STAR-CCM+, were defined by Launder and Sharma in 1974 and they are

$$C_\mu = 0.09, \quad C_{\varepsilon 1} = 1.44, \quad C_{\varepsilon 1} = 1.92, \quad \sigma_k = 1, \quad \sigma_\varepsilon = 1.3 \tag{2.26}$$

This is the standard k-ε model, the most popular model in industrial applications for its robustness and good level of convergence. However it has several limitations and it does not work very accurately for flow fields with adverse pressure gradients, strong curvature, separation or recirculating zones because of the nature of the equation for ε and because the Boussinesq hypothesis loses its validity. To achieve good results for different flow fields, this model has been revisited with many modifications, also adding wall functions to resolve the boundary layer.

2.4.2 k-ω model

As the flow field around the car is quite complex because of separation at the rear, wheels' wake and other issues, an optimisation study requires a high level of accuracy, therefore a k-ω model would be suitable for the primal simulation, in particular Menter's SST k-ω. Among its main advantages over the other models, there are a better performance in computation of boundary layer flows under adverse pressure gradients even in the logarithmic region and its application throughout the viscous sub-layer without any modifications.

Like the one showed in the previous section, it is composed by two equations, one for the turbulent kinetic energy and the other one for the specific dissipation rate ω, defined as

$$\omega \approx \frac{\varepsilon}{k} \tag{2.27}$$

This quantity has the same dimension of the vorticity, i.e. $[s^{-1}]$, so it represents a sort of characteristic frequency of fluctuations and its reciprocal is the time scale of the turbulent dissipation.

In the technical memorandum [10] and in the paper [11] Menter derives its SST model starting from the k-ε model and k-ω model proposed by Wilcox. In the outer region of the boundary layer Wilcox's model shows a strong sensitivity to the arbitrary values for ω in the free-stream, and this is a relevant problem in particular for the inlet boundary conditions that have to be imposed. To avoid this problem and to implement a model with

all the advantages guaranteed by the others, Menter proposed to unit the standard k-ω model and the standard k-ε model manipulating them in some manner using a blending function F_1. This function is equal to one in the inner region of the boundary layer, activating the k-ω model, while it gradually becomes equal to zero in the outer region where the k-ϵ model is valid, overcoming the sensitivity of ω to free-stream conditions. The following equations form the SST k-ω model

$$\frac{\partial k}{\partial t} + \overline{U}_j \frac{\partial k}{\partial x_j} = -\overline{u_i' u_j'} \frac{\partial \overline{U}_i}{\partial x_j} - \beta \omega k + \frac{\partial}{\partial x_j} \left[(\nu + \sigma_k \nu_T) \frac{\partial k}{x_j} \right] \tag{2.28}$$

$$\frac{\partial \omega}{\partial t} + \overline{U}_j \frac{\partial \omega}{\partial x_j} = -\gamma \frac{\omega}{k} \overline{u_i' u_j'} \frac{\partial \overline{U}_i}{\partial x_j} - \beta \omega^2 + \frac{\partial}{\partial x_j} \left[(\nu + \sigma_\omega \nu_T) \frac{\partial \omega}{x_j} \right] + P_\omega \tag{2.29}$$

where the production term P_ω is defined as

$$P_\omega = 2(1 - F_1)\sigma_{\omega_2} \frac{1}{\omega} \frac{\partial k}{\partial x_j} \frac{\partial \omega}{\partial x_j} \tag{2.30}$$

A peculiarity of this model is the presence of a new term represented by the dot product between the gradients of k and ω, defined as the cross-diffusion term.

A detailed presentation of the general formulation of this model with all the coefficients is showed in STAR-CCM+ documentation [12].

The acronym SST stands for Shear Stress Transport, in fact this model accounts for the transport of the principal component of the Reynolds stress tensor, i.e. $-\rho\overline{u'v'}$, allowing to predict in a better way the anisotropy of turbulence. This expedient requires a new definition for the turbulent viscosity, which is proportional to the turbulent kinetic energy and is defined as follows

$$\nu_T = \frac{a_1 k}{\max\left(a_1 \omega,\, F_2 \dfrac{\partial u}{\partial y} \right)} \tag{2.31}$$

where a_1 is a constant and F_2 is a function that is one for boundary-layer flows and zero for free shear flows.

Thanks to these features, Menter's model is widely used in aerospace applications and it would be preferable for complex aerodynamic simulations. However generally it is more difficult to converge than the k-ε model and it requires a very refined mesh in the viscous sub-layer.

2.5 Near-wall treatment

As the walls are a source of vorticity in most flow fields, the computation of the boundary layer flows in proximity of this zone must be as accurate as possible. The boundary layer can be divided into an inner region and an outer region. Moreover the inner region can be split up into three sublayers, with different features: the viscous sublayer, the buffer layer and the log-law layer.

At this point two variables are introduced to represent the characteristic scales of viscous fluctuations in the boundary layer; they are the so called friction velocity u_τ and the length scale l_w, defined as follows

$$u_\tau = \sqrt{\frac{\tau_w}{\rho}} \qquad l_w = \frac{\nu}{u_\tau} \tag{2.32}$$

where τ_w is the viscous stress at wall computed with the Newton's law. Thus in the inner region of the boundary layer these two variables can be used to form two non-dimensional velocity and length scales, respectively defined as u^+ and y^+, with the latter representing the non-dimensional wall distance and it is used to compute the extent of each sublayer.

$$u^+ = \frac{U}{u_\tau} \qquad y^+ = \frac{u_\tau y}{\nu} \tag{2.33}$$

They are called inner variables or wall variables. It is interesting noting that y^+ has the same form of the Reynolds number.

The viscous sublayer is the closest to the wall. Here the viscous stresses dominate over the Reynolds stresses and the flow is almost laminar. The velocity profile is linear according to the wall law

$$u^+ = y^+ \tag{2.34}$$

For high Reynolds numbers the extent of this sublayer is independent from the external flows and it spreads from the wall to a non-dimensional distance of about $y^+ \simeq 5$.

In the log-law layer, where Reynolds stresses dominate the turbulent flow, the relation between the two wall variables is expressed by the following logarithmic law

$$u^+ = \frac{1}{K} \ln(y^+) + C \tag{2.35}$$

where $K = 0.41$ is the Von Karman constant and C is another constant equal to 5. The extent of the log-law layer is dependent from the Reynolds number, and it increases as the Reynolds number increases. Generally it spreads from $y^+ \simeq 30$ to a distance equal to 0.2δ, where δ is defined as the boundary layer thickness.

The buffer layer is a transitional layer between the others where both viscous stresses and Reynolds stresses are important and there isn't a valid universal law. For this reason is preferable to create a mesh where no cell centres fall into this layer. The Figure 2.1 shows the structure of velocity profile in the inner boundary layer.

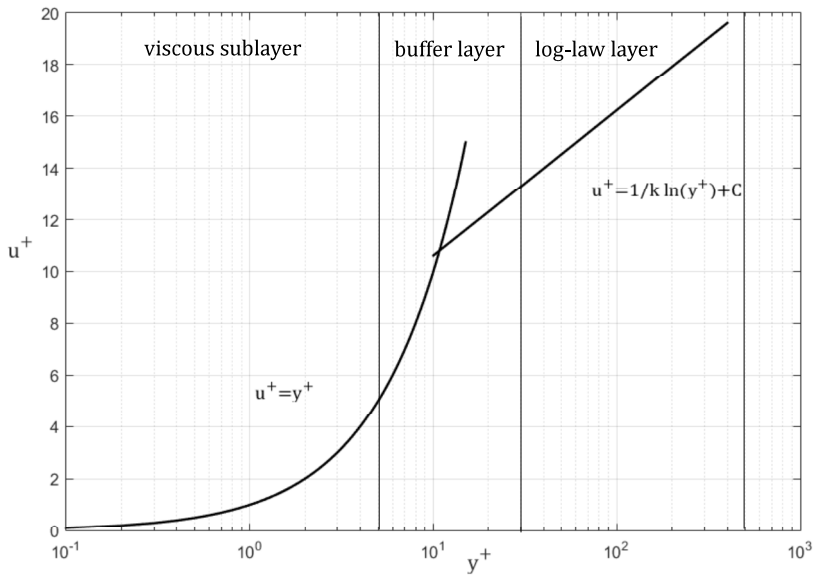

Figure 2.1. Wall laws in the inner layer.

STAR-CCM+ provides three types of wall treatment: low-y^+, high-y^+ and all-y^+. The latter resolves the viscous sublayer where the mesh is fine as the low-y^+ treatment does and it behaves like the high-y^+ treatment for coarse mesh where the first cell falls at $y^+ > 30$. It uses blending functions where cells lie in the buffer layer; however it would be worthwhile avoiding this situation.

Chapter 3

Adjoint method

In this chapter a brief discussion on the adjoint method is proposed, without entering too much in mathematical details because it is beyond the purpose of this thesis.

3.1 Analysis workflows

In Figures 3.1 and 3.2 the differences between a traditional approach to design and the adjoint approach are showed. Traditional approach to aerodynamic optimisation considers the generation of a DOE (Design of Experiments) during the early design phase and by means of several algorithms the influence of many parameters on the initial design is evaluated in order to reach a specific objective. Therefore by varying the input conditions it is possible to examine the cause-effect relationship and determine the optimal solution. When the number of parameters is high, this process can be very time consuming and the computational effort grows dramatically. Even simulating and comparing many different model configurations can lead to unacceptable development times and limit the design exploration space.

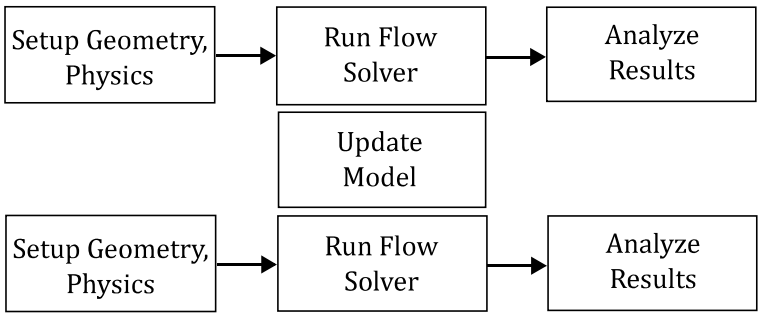

Figure 3.1. Traditional analysis workflow.

The adjoint method is a useful tool to predict the influence of a certain number of design parameters or boundary conditions on specific quantities of interest, defined as objective or cost functions. An adjoint simulation requires the computation of the steady-state solution that represents the so called *primal solution*, and the computation of the gradient or sensitivity of the cost function. The results provide the starting point for an optimisation cycle, that can be performed on the same simulation workflow, without preparing different cases.

The main advantage of the adjoint approach is the method's cost independence from the number of design variables, so it is possible to explore a potentially infinite design space. With respect to traditional optimisation approaches, fewer design iterations are needed to reach the best configuration, saving a lot of time, fundamental in the product development. The adjoint method offers a guidance towards the improvement of the interested performance by a shape optimisation, thanks to the sensitivity analysis computed with respect to the mesh node displacement. Even computing the adjoint with regard to physical quantities such as continuity and momentum is possible, allowing to evaluate how the cost function is sensitive to local changes in mass and in momentum in each spatial direction within the domain.

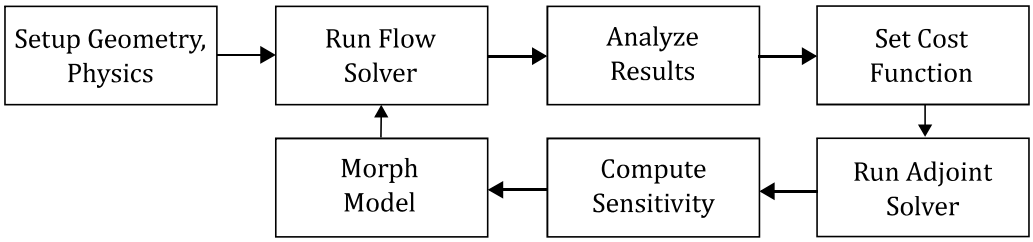

Figure 3.2. Adjoint method workflow.

3.2 Mathematical formulation

Adjoint methods are formulated following two different approaches, continuous and discrete approach. From the mathematical point of view they differ only in the way to obtain the same final system of equations. Figure 3.3 summarizes the steps followed in two approaches. Both formulations start from the system of the governing PDEs. In the discrete approach these equations are first discretise and then the discrete adjoint equations are obtained with some operations; in the continuous approach the adjoint equations are formulated directly from the governing flow equations and then discretised together with

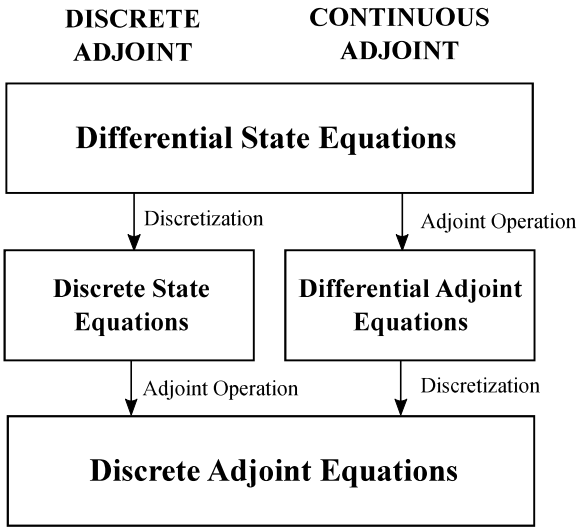

Figure 3.3. Difference between adjoint approaches.

their boundary conditions and solved. Their mathematical formulation is very challenging with respect to traditional gradient-based methods, but when the number of design parameters involved is high, the initial effort is justified by the cost independence of the adjoint. For simple cases the computational effort is similar for both approaches, but for industrial cases relative advantages and disadvantages should be evaluated.

3.2.1 Continuous Approach

We recall the RANS equations in steady-state and non-conservative form for incompressible flows. The average sign is omitted for the sake of simplicity

$$\frac{\partial U_i}{\partial x_i} = 0 \tag{3.1}$$

$$U_j \frac{\partial U_i}{\partial x_j} + \frac{\partial p}{\partial x_i} - \frac{\partial}{\partial x_j}\left[(\nu + \nu_T)\left(\frac{\partial U_i}{\partial x_j} + \frac{\partial U_j}{\partial x_i}\right)\right] = 0 \tag{3.2}$$

where U_i and p, neglecting the turbulent kinetic energy contribution, are respectively the primal velocity and the primal pressure. Before deriving the adjoint equations, a cost function must be defined. It is a combination of a surface integral on the domain boundary and a volume integral in the entire domain Ω

$$F = \int_S F_s dS + \int_\Omega F_\Omega d\Omega \tag{3.3}$$

For each cost function to optimise, an adjoint equation has to be formulated. With some manipulations, the adjoint equation system is the following one, from reference [4],

$$\frac{\partial V_i}{\partial x_i} - \frac{\partial F}{\partial p} = 0 \tag{3.4}$$

$$-U_j \frac{\partial V_i}{\partial x_j} + V_j \frac{\partial U_j}{\partial x_i} + \frac{\partial q}{\partial x_i} - \frac{\partial}{\partial x_j}\left[(\nu + \nu_T)\left(\frac{\partial V_i}{\partial x_j} + \frac{\partial V_j}{\partial x_i}\right)\right] + \frac{\partial F}{\partial U_i} = 0 \tag{3.5}$$

where V_i and q are respectively the so called adjoint velocity and the adjoint pressure. The second term in equation (3.5) is defined as Adjoint Transpose Convection and it is a source of instability in the computation. The shape sensitivity with regard to normal displacement of each cell node can be computed after solving both primal and adjoint systems of equations. The surface sensitivity map can be exported and used in an external software as deformation parameter. Instead if the optimisation loop is performed using a grid of control points, the sensitivity of the cost function with regard to these points is computed applying the chain rule as follows

$$\frac{\partial F}{\partial b} = \frac{\partial F}{\partial x_m} \cdot \frac{\partial x_m}{\partial b} \tag{3.6}$$

where b are the coordinates of the points and x_m are the coordinates of the mesh nodes.

In this derivation turbulence model equations are not considered, in fact the turbulent viscosity is assumed to be constant with regard to variations in the design variables and it is treated as passive quantity, according to the frozen turbulence assumption.

3.2.2 Discrete Approach

In our case the cost function, defined as L, is the aerodynamic drag that has to be minimised. In general it is a non-linear function of a set of flow variables computed at discrete grid points, representing the solution $\mathbf{Q} = [p, \mathbf{V}]^T$ of the governing equations, and of a set of design parameters $\mathbf{D}$ that define the coordinates of the mesh by means of a function $\mathbf{X}(\mathbf{D})$. What we want to study is how the cost function is influenced by a perturbation in the design variables $\mathbf{D}$, in this case the external shape of the vehicle, and so in the flow field and to find a set of them that minimises the cost function. The cost function is computed following a sequence of operations, ($\mathbf{X}(\mathbf{D})$, $\mathbf{Q}(\mathbf{X})$, $L(\mathbf{Q}, \mathbf{X})$). The adjoint simulation follows the reverse sequence, because starting from the sensitivity of the cost function it has to determine a new mesh depending on the design parameters.

In order to minimise the cost function with design modifications instead of boundary conditions change, the total derivative in the following expression provides the sensitivity of L with regard to the design parameters and it is obtained with the chain rule applied

to the previous operations,

$$\frac{dL}{d\mathbf{D}} = \left[\frac{\partial L}{\partial \mathbf{X}} + \frac{\partial L}{\partial \mathbf{Q}}\frac{\partial \mathbf{Q}}{\partial \mathbf{X}}\right]\frac{d\mathbf{X}}{d\mathbf{D}} \tag{3.7}$$

The term $d\mathbf{X}/d\mathbf{D}$ is the Jacobian of the function $\mathbf{X}(\mathbf{D})$, defined as J_X and each row of the matrix represents the gradient of each mesh coordinate with respect to all the design parameters. For a large number of design parameters the adjoint operation requires a great effort in terms of memory, therefore a different approach is followed to reduce the computation time, taking the transpose of the derivative of the system for the given L

$$\frac{dL}{d\mathbf{D}}^T = \frac{d\mathbf{X}}{d\mathbf{D}}^T\left[\frac{\partial L}{\partial \mathbf{X}}^T + \frac{\partial \mathbf{Q}}{\partial \mathbf{X}}^T\frac{\partial L}{\partial \mathbf{Q}}^T\right] \tag{3.8}$$

This gradient is used to solve the shape optimisation problem and it is the starting point to define the new values of the design parameters. In other words, the morpher tool deforms the mesh coordinates according to these values. The terms in square brackets represent the sensitivity of the cost function with regard to the coordinates of the volume mesh vertices. This function is computed after the determination of the sensitivity of L with regard to the flow solution $\partial L^T/\partial \mathbf{Q}$, that is the input for the adjoint solver. This approach is valid even when the cost functions are more than one, the gradient is computed for each specified cost function.

3.2.3 Advantages and disadvantages of two approaches

The final aim of the adjoint method is to compute the gradient of a specified cost function with regard to design variables. There are conceptual differences between the discrete and continuous approach and each one has its own advantages and disadvantages that are summarized in this section.

With the discrete approach the gradient of any discrete cost function is computed exactly, but the computational cost can be considerably higher than the primal solution and this could make preferable the other approach [4]. The continuous approach requires less memory and because one is theoretically free to chose any discretisation scheme for the adjoint equations, it would have a simpler implementation [6]. The greater challenge can be obtaining the final equations depending from the complexity of the primal equation system [4]. With this approach the cost function is analytically exact, starting from a continuous formulation, but the discrete gradient is an approximation strictly depending on the discretisation scheme [13]. Therefore there is a slight inconsistency between two approaches. However, if the mesh is sufficiently refined, both approaches can lead to the

same result [6].

Another drawback common to gradient-based methods is that if the cost function has more than one minimum, then the gradient approach will generally converge to the nearest local minimum. In the case of study it could be reasonable thinking that the aerodynamic configuration of the vehicle is already near to the best shape.

3.3 Adjoint solver

The discretisation scheme used to obtain the equation system can be first-order or second-order. Though a second-order scheme provides a better accuracy it can be very unstable for industrial problems, therefore a first-order scheme is chosen in order to guarantee robustness and convergence.

The adjoint equations form a linear system solved with an iterative defect-correction algorithm. The default algorithm implemented within the solver doesn't guarantee an adequate convergence for this case, in fact an adjoint analysis requires that residuals approach machine precision. As alternative, the software provides two acceleration drivers: Restarted GMRES and Flexible GMRES, where the acronym stands for "generalized minimal residual". These are modern iterative methods based on the Krylov subspace to find eigenvalues of large sparse matrices and solve large linear systems. Enhancing the convergence using the Restarted GMRES solver is verified to be the suitable practice, resulting in an increase of robustness but also of computation time and memory requirements. With these features the adjoint method has a computational effort approximately double with respect to the primal simulation.

Table 3.3 shows the setup followed in all the simulations. For the Krylov space dimension the number between brackets refers to that used for simulations running with k-ω model, that requires a more robust setup.

Table 3.1. Adjoint solver setup.

Adjoint Acceleration Selection	**Restarted GMRES**
Krylov Space Dimension	**30(50)**
Number of correction sweeps	**5**
Courant Number	**100**

Chapter 4

Case description

4.1 Fiat Tipo

The model chosen as subject of this thesis is the Fiat Tipo 5 Porte, whose 3D geometry is shown in Figure 4.1. It falls in the category of those cars defined as "hatchback".

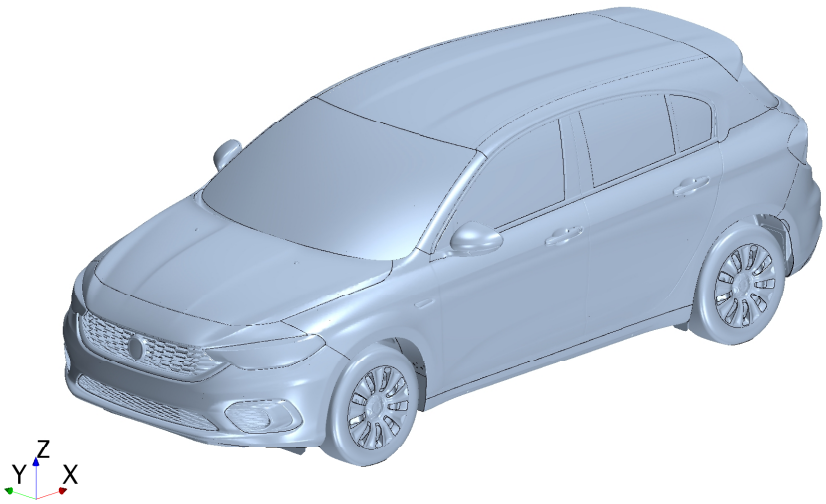

Figure 4.1. Fiat Tipo Hatchback, 3D model.

In general one of the major contributes to drag generation is due to the flow separation and the complex flow field in the wake at the rear. The main aerodynamic problem related to an hatchback vehicle is the formation of vortices depending on the inclination of the slanted surface of the rear window with respect to a horizontal line. Vortices rise in consequence of local shear, pressure or velocity difference in the flow field. A typical

situation of vortex-dominated flow is displayed in Figure 4.2 and it is evident for a slant-angle range of 10°-30°, [14]. In this condition the flow separates only at the rear base and the velocities induced by the vortices on slant surface generate an intense suction force, increasing dramatically the lift. Moreover, approaching to 30°, that represents the critical angle, there is a remarkable source of drag because the force normal to the slanted surface has a component parallel to the flow and in the opposite direction of the car motion. About above 30° vortices break down and the flow separates, resulting in a quasi-uniform

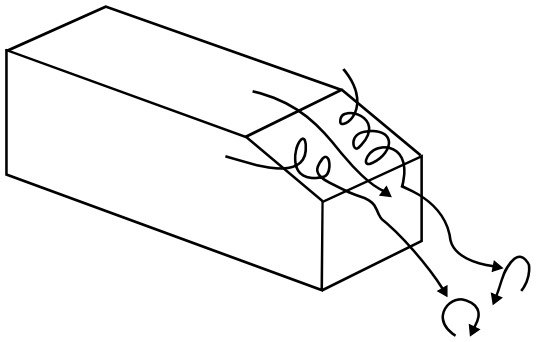

Figure 4.2. Slanted rear.

pressure distribution on the whole trunk and in a recirculating wake configuration as shown in Figure 4.3, with an improvement in drag. Therefore the design of an hatchback

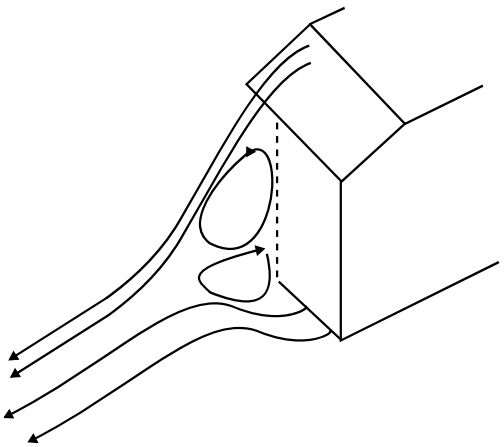

Figure 4.3. Wake vortices.

model has to take into account this phenomenology and the rear window would have an inclination at least equal to 35°. The typical solution concerns the installation of a spoiler, that forces the flow to separate at the trailing edge, as though the rear window has an inclination close to 90°.

Also the inclination of the spoiler has to be taken into account, because a good compromise has to guarantee an adequate reduction of rear-axle lift without increasing drag too much. For all these reasons during the optimisation process a particular attention is focused on the spoiler configuration and on C pillars, essential to control flow separation at the rear.

The geometry on which simulations are performed consists of the entire vehicle, including all external details and all the mechanical parts like the engine, brake and suspension systems. For time reasons it was not possible to verify the practicability of the adjoint on other vehicles.

4.2 Mesh setup

Finding the right mesh setup to ensure the convergence of the adjoint solver is not easy. The complexity of the geometries and the adjoint sensitivity to potential imperfections of the computational grid require a volume mesh with very high quality, more than that prepared for only primal simulations. Therefore the realized mesh for our adjoint simulation is different from that generally used for external aerodynamics simulations. Two meshing models are used, the Trimmer Mesher and the Prism Layer Mesher, but it is necessary to customize them to improve mesh quality in zones with very fine details.

From the point of view of the Prism Layer Mesher, a low-y^+ mesh is generated on the external surfaces where it is necessary to resolve the boundary layer with high accuracy, in order to compute also the correct contribution of viscous stresses on drag generation. Even the tyres are discretised with a refined mesh, but rims, caps and MRF have a high-y^+ mesh, because of the complexity of the geometries of these regions.

A high-y^+ mesh is chosen for baffles, that are surfaces with zero-thickness, air intakes that have a complex geometry and it is difficult to generate a detailed boundary layer on them, and for the underbody. Because of the complex geometry of the underbody, to avoid the generation of a great amount of drag due to a disturbed flow, most of parts of this component are within the wake of the front dam, thus it is not necessary to refine too much the boundary layer. Figure 4.4 shows the wall y^+, that is the non dimensional distance of the first cell center from the wall, on the vehicle.

The resultant mesh has more than 100 millions of cells. Table 4.1 provides the complete setup of the surface controls expressed as percentage of the base size. A custom mesh control allows to refine or coarsen the mesh applying it to several surfaces or volumes.

Though in the standard procedure for the primal simulation some bad cells within a certain target are removed, when an adjoint run has to be performed, they have to not be

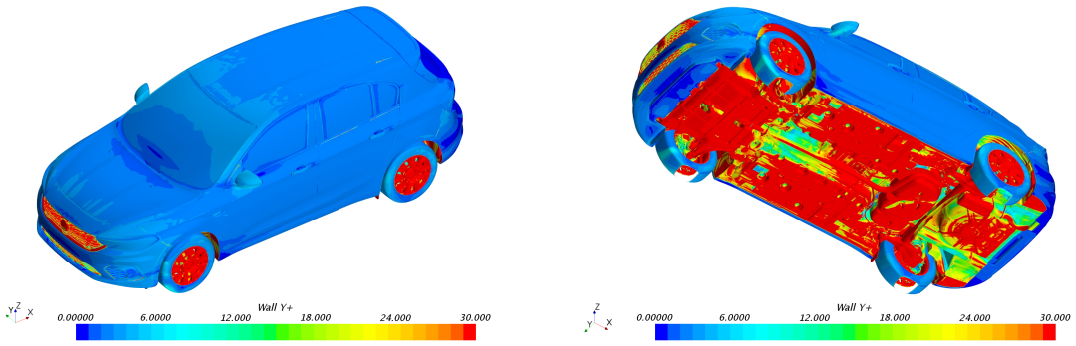

(a) *External surfaces.* (b) *Underbody.*

Figure 4.4. Wall y^+ on the vehicle.

Table 4.1. Mesh custom controls as percentage of the base size.

	Target Surface Size	Minimum Surface Size
External	100	50
Underbody	100	25
Underhood	100	25
Tyres	50	50
Rims and caps	50	25

deleted because numerical errors would spread to the adjacent cells causing problems during the computation. Therefore only cells with negative volume, if any, must be removed. In fact while the primal simulation can be more tolerant to imperfections of the mesh, the adjoint solver is much more sensitive to them. This is true in particular for complex geometries and for detached flows. Because of this weakness of the solver, robustness in computation is preferred despite a certain loss of accuracy [3].

In Figure 4.5 is shown the mesh at the symmetry plane of the vehicle. On the car there are several refinement blocks, with lower mesh size, to compute accurately the flow field. Wheels, mirrors, spoiler's wake has to be well captured by the mesh and also A pillars, where vortices born and C pillars where the flow can separate, have to be refined both in surface and volume mesh.

The volume mesh is a trimmed one. It is an unstructured grid composed by hexahedral cells, cut with the geometry surface and characterized by low skewness. This mesher allows the realization of a high-quality grid also for complex problems. Growth rates can be set to control the transition of cell sizes from small to large. In STAR-CCM+ one of its

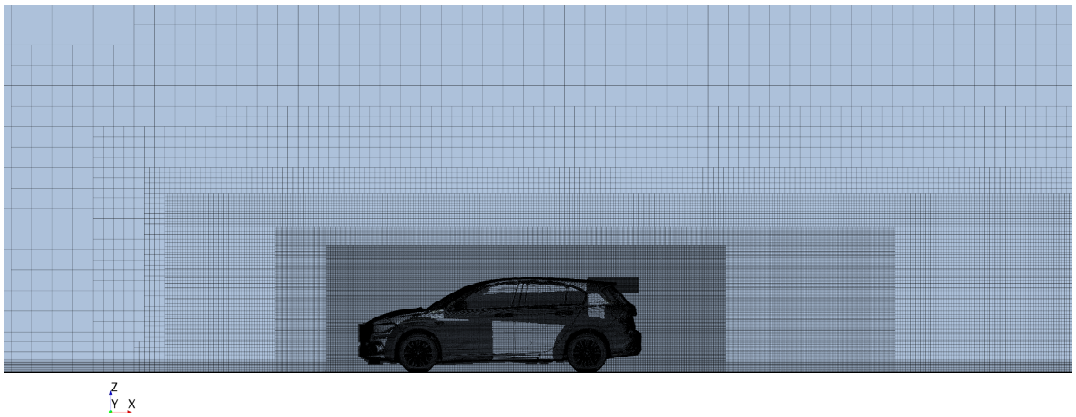

Figure 4.5. Trimmed mesh at the symmetry plane.

advantages is the possibility to use more parallel cores to generate it with respect to a polyhedral mesh.

4.3 Boundary conditions

The fluid domain for external aerodynamics simulations is defined as "Open Air". It must represent as well as possible the real conditions in which the vehicle operates on the road, therefore its dimensions are big enough to avoid any sort of blockage. The mathematical model is completed specifying the boundary conditions on the domain, depending on the flow situations. The boundary conditions allow to define where the flow enters or leaves the computational domain and its behaviour on the walls.

The inflow condition is a *velocity inlet*, where the velocity magnitude and direction of the flow are specified. In our case the air velocity is uniform and it is equal to 38.89 m/s. The outlet is a *pressure outlet*, where the pressure is specified and its value is constant and equal to the reference one. On the *walls* of the domain a *slip condition* is imposed, therefore the flow slides along the wall without any shear forces. The entire floor slips at the same velocity of the air entering from the inlet at 38.89 m/s. A tangential velocity specification is imposed to each wheel in order to simulate their rotation, creating a Moving Reference Frame (MRF).

4.4 Solvers

As at speed of 38.89 m/s the Mach number is less than 0.3, compressible effects are negligible, therefore the simulations are performed using a *constant density* model for the air, neglecting the energy equation. The air has the density equal to $\rho = 1.225\,kg/m^3$ and the dynamic viscosity is $\mu = 1.79 \cdot 10^{-5}\,Pa \cdot s$.

The integral conservation equations of mass and momentum are solved in a coupled manner. While the segregated flow solver uses a pressure-correction equation to compute the right velocity field that fulfils the kinematic constraint imposed by the continuity equation, solving the equations iteratively, the *coupled solver* provides a converged solution in terms of velocity field and pressure solving conservation equations simultaneously.

From the point of view of the time discretisation, the coupled system of equations is solved with an *implicit* time-integration scheme. For steady-state simulations the time-stepping is performed until a quasi steady-state solution is obtained. When an explicit approach is followed, the discrete equations provide the value of the fluid dynamic quantities at a certain time level $n + 1$ knowing the values at time level n, and this holds for each grid node, solving the equations by marching in steps of time. The solution in this case is immediate. The implicit approach requires the solution of a system of algebraic equations, where all the quantities at time level $n + 1$ are expressed in terms of other unknown quantities at both time levels n and $n + 1$. Solving the system provides the solution at all the grid points simultaneously. Clearly this approach is more complicated and it would require more computational and implementation effort with respect to the explicit one. However its main advantage is that it is unconditionally stable, therefore a larger time step can be used if the steady-state solution is researched, without losing stability and timewise accuracy. For this reason the Courant number, that represents the stability condition, can be very high reducing computing time.

4.5 Optimisation Methodologies

Two different ways are followed to morph the external shapes. The aim is finding the best procedure in terms of quality and computational time. Results of the primal simulation in terms of drag coefficient are the starting point for the optimisation loop, performed using both ANSA and STAR-CCM+ morphing tools and capabilities. The robustness of the adjoint solution relies on the fidelity of the primal flow field, therefore also a comparison between k-ε and k-ω model is carried out, in order to establish what model is the most reliable.

4.5.1 Design guidelines via surface sensitivity

After the primal simulation and the adjoint run, computing the surface sensitivity of the cost function is the first step in an optimisation cycle. It provides the information necessary to individuate those areas that are the most sensitive to geometry modifications and that can have the major impact on the aerodynamic drag. Though there are some zones for

which the experience can suggest *qualitatively* how to intervene, surface sensitivity is a useful tool not only for those parts that are difficult to change only looking at the primal results, but also because it provides a *quantitative* information about the impact of shape changes on the drag. However, in this case the optimisation is a fine-tuning operation because probably the vehicle is already close to its optimal shape, therefore it is difficult to expect substantial variations in the final result.

In order to explain how results have to be interpreted, Figure 4.6 shows the surface sensitivity with regard to the normal displacement of the spoiler, computed for each node of the surface mesh. Remembering that the normal vector is considered positive if it enters into the fluid domain, negative values, corresponding to blue areas, indicate that pulling outwards the surface, i.e. in the direction of the normal, the drag would decrease. Positive values, corresponding to red areas, suggest that the surface has to be pushed inwards to reduce drag. For the example in figure, sensitivity drives to a reduction of the spoiler inclination.

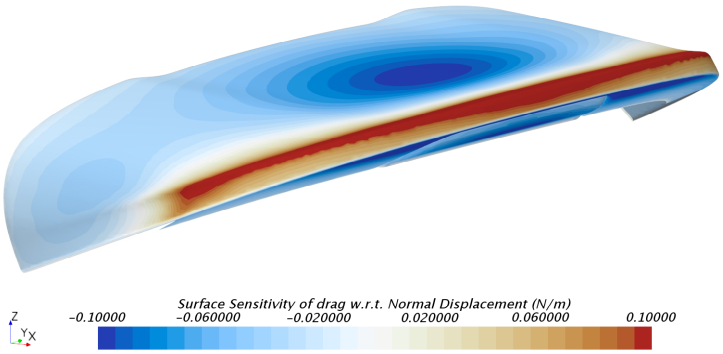

Figure 4.6. Surface Sensitivity [N/m] of Drag with regard to Normal Displacement for spoiler.

4.5.2 Morphing with ANSA

A practicable methodology concerns the possibility to perform the morphing using an external software. In this case the morphing procedure is carried out with ANSA Pre-processor, a computer-aided engineering software developed by Beta CAE Systems, that associates the CAD geometry with a FE (Finite Element) mesh. It is widely used in automotive industries to provide a detailed surface mesh as basis for CFD purposes. The procedure takes advantage of the powerful morphing tool of ANSA, in this case morphing operations are performed directly on the surface mesh using the results in terms of surface sensitivity as a deform map. Other methods allow a parametric control of the shape

changes using the Direct Fit Morph function or morphing boxes, as explained in [15] and [3].

Surface sensitivity is extracted from STAR-CCM+ as a table of values with respect to the three spatial directions. ANSA uses these values as a deform map of nodal displacements, translating them into changes of the geometry surfaces. The software allows to control the morphing operation choosing the maximum displacement and the number of displacement vectors involved. Selecting entities which have to be morphed and elements in their proximity would guarantee a good quality result avoiding intersections.

Though ANSA provides a good quality result, the main drawback of this methodology is the time consuming in reimporting the morphed geometry into STAR-CCM+ and remeshing it before performing a new primal simulation to verify the effect of the modifications.

4.5.3 Morphing with STAR-CCM+

In order to overcome this drawback and to take advantage of the capabilities of STAR-CCM+, an entire optimisation cycle in the same simulation file is experimented. In this case, after the solution of the primal flow field and the adjoint system, the computation of the surface sensitivity has only the aim to indicate where the cost function is more sensitive to changes in volume mesh and thus in shapes.

Taking into account this indication, several control points are inserted close to surfaces that have to be morphed. The software uses these points to deform the volume mesh. Control points have to be close enough to the boundary to be deformed in order to have a sufficient influence on it, but with enough offset from the surface to ensure smooth deformations. An example is provided in Figure 4.7, where two bi-dimensional lattices are located respectively about 5 cm and 10 cm over the spoiler. The deformation is applied to the closest points, whereas the displacement associated with the highest lattice of points is forced to be zero to avoid excessive deformations of the mesh, losing quality.

On these control points the software computes the mesh sensitivity, providing the cost function gradient defined as *Adjoint of drag with regard to position* and it has the following expression

$$\frac{dL^T}{d\mathbf{D}} = \frac{d\mathbf{X}^T}{d\mathbf{D}} \frac{dL^T}{d\mathbf{X}} \tag{4.1}$$

where $\mathbf{D}$ are the design parameters that define the mesh coordinates $\mathbf{X}(\mathbf{D})$ and L is the cost function. The morpher deforms the mesh according to the values provided by this sensitivity. These values are always positive because they indicates the required deformation to increase the cost function. Therefore, in order to reduce the aerodynamic drag, the displacement function associated with each set of control points has to generate

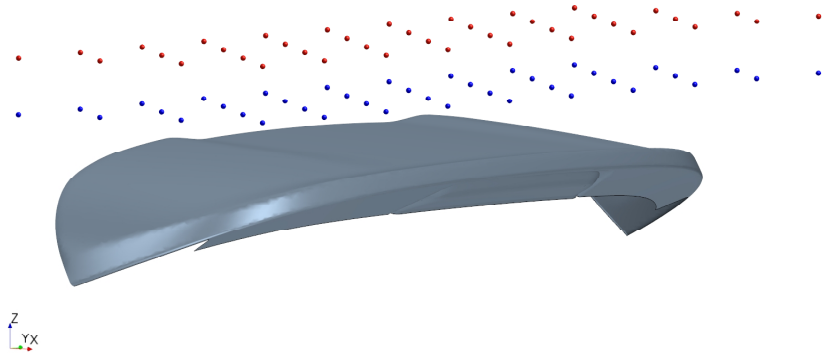

Figure 4.7. Lattice of control points on the spoiler.

a negative displacement. An example of this vector field is shown in Figure 4.8 and it represents the gradient computed on the first lattice of points over the spoiler. A similarity with the advice given by the surface sensitivity can be noted, in fact also the mesh sensitivity indicates that the trailing edge has to be bent down.

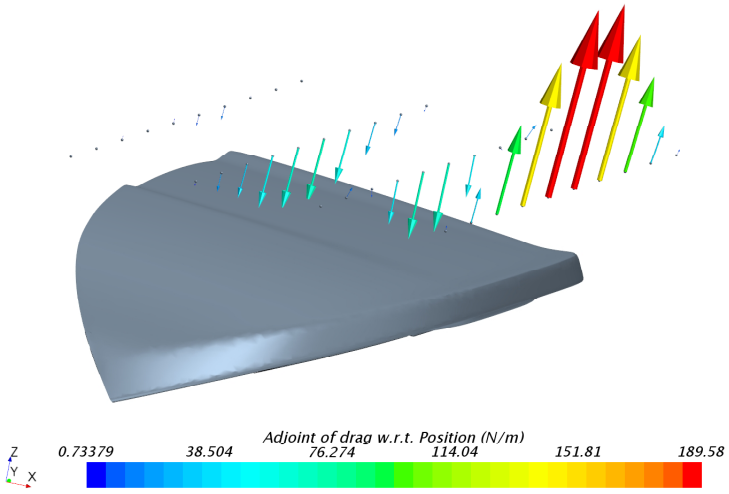

Figure 4.8. Mesh sensitivity computed on control points.

A simple *first-order steepest descent algorithm*, with a low computational cost, is used to morph the mesh with the following formulation

$$\mathbf{X} = \mathbf{X}^0 - \alpha \frac{dL^T}{d\mathbf{D}} \tag{4.2}$$

where $\mathbf{X}^0$ is the first or, in general, the previous mesh and α is the step size that defines a fraction of the gradient. The surface geometry is modified by changes in the design parameters. In STAR-CCM+ all the deformations are stored in a function defined as *Cumulative Morpher Displacement*.

As the morpher acts directly on the volume mesh, there is no need to remesh the model, so the verification of the performance of the new shape can be performed running again the primal solver. On the other hand this feature represents also the main disadvantage of this workflow, in fact volume mesh tends to lose quality for each optimisation cycle.

Chapter 5

Results

In this chapter the results of both optimisation methodologies are collected. The attention is focused on the drag coefficient, that represents the non-dimensional form of the aerodynamic drag

$$C_D = \frac{D}{\frac{1}{2}\rho V_\infty^2 A}$$

where V_∞ is the air velocity and A is the frontal area of the car. The first primal simulation provides the reference value of C_D; all the subsequent coefficients are expressed as percentage of it. When we talk about the aerodynamic drag we refer to the total rate of decrease in momentum in the direction of the motion. A global measurement of the drag includes contributes of both pressure and viscous drag. Pressure drag, also defined as form drag, is the integral of the pressure forces acting normal to surfaces and it is the major contribute. Viscous drag represents the surface integral of the shear stress components aligned with the undisturbed flow and for a car it is about one tenth of the total drag.

5.1 Primal simulation results

The following results refer to the fluid dynamic simulation based on the Standard k-ε model, that for our case it has proved as the most robust. A first overview on the flow field around the car is provided by the pressure coefficient. It represents in non-dimensional form the difference between the pressure acting on vehicle surfaces and the one of the undisturbed flow, defined as p_∞

$$C_p = \frac{p - p_\infty}{\frac{1}{2}\rho V_\infty^2} \tag{5.1}$$

Figure 5.1 shows the C_p distribution on the external surfaces and on the underbody, clipping it at zero, when $p = p_\infty$. Clearly the front end of the car is a stagnation zone,

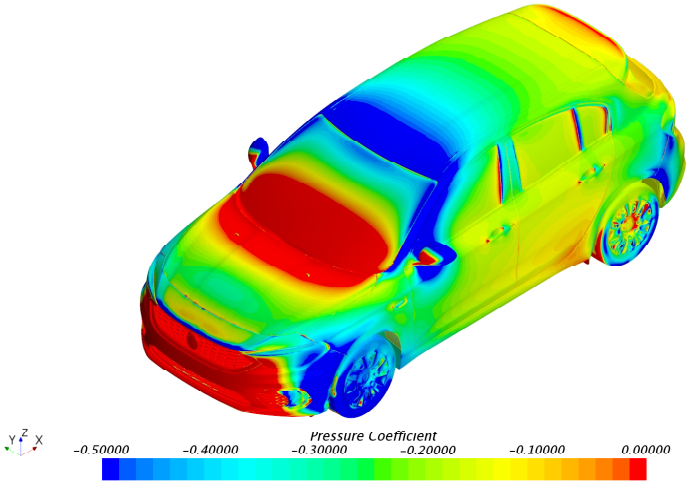

(a) *External surfaces.*

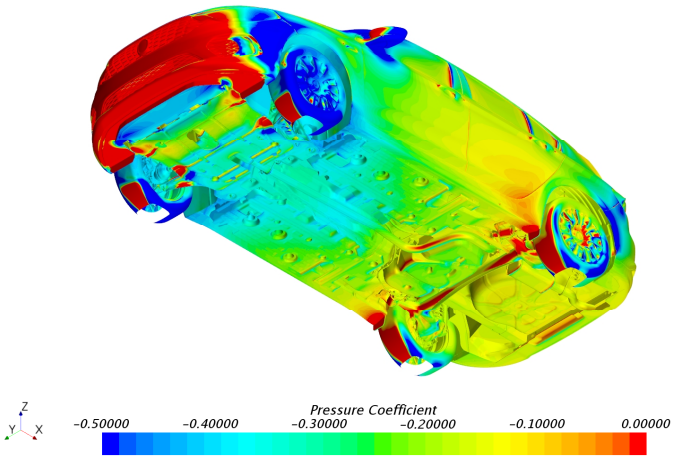

(b) *Underbody.*

Figure 5.1. Pressure coefficient on car surfaces.

where the coefficient reaches its maximum value, equal to one. Other overpressure zones are on the mirrors, on part of the bonnet and the windscreen where the flow slows down, and at the trailing edge of the spoiler. Negative values represent suction zones, and these have to be reduced at the trunk, where the pressure distribution is shown in Figure 5.2, in order to decrease the drag. Also most of the underbody exhibits low pressure, because the front dam forces the flow to separate in order to avoid complex turbulent structures due to the exposure of mechanical components. Moreover the low pressure zone caused

by detached flow helps to generate a certain amount of negative vertical force.

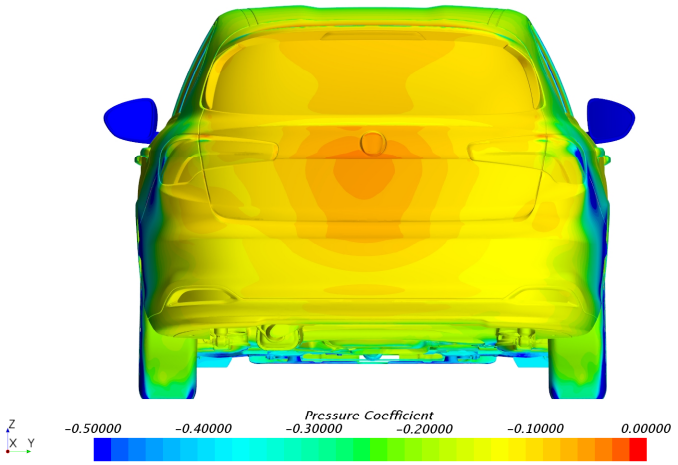

Figure 5.2. Pressure coefficient at the rear of the car.

In Figure 5.3 the velocity magnitude in the symmetry plane is shown, highlighting how the flow separates immediately at the trailing edge of the spoiler, creating a wide low pressure zone in the wake, that displays a behaviour like that described in the previous chapter, with a big recirculating zone where the mean velocity is very low. Separation

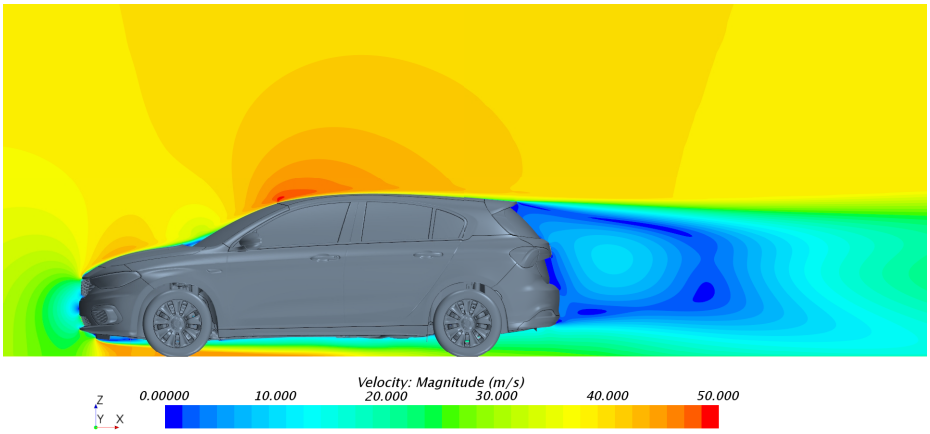

Figure 5.3. Velocity magnitude in the symmetry plane $y = 0$ of the baseline.

is evident also looking at the skin friction coefficient distribution on the rear surfaces in Figure 5.4, where its value approaches zero. The skin friction coefficient is defined as follows

$$C_f = \frac{\tau_w}{\frac{1}{2}\rho V_\infty^2} \tag{5.2}$$

where τ_w is the shear stress magnitude at wall, therefore C_f depends on the velocity gradients. If the flow is separated, the mean gradients are zero or close to zero.

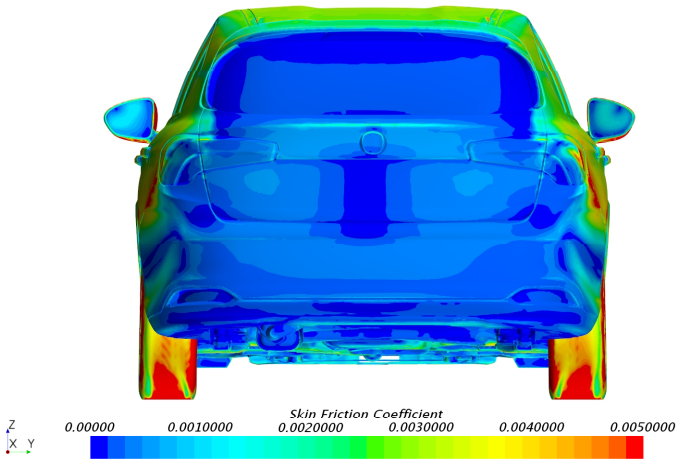

Figure 5.4. Skin friction coefficient at the rear.

In Figure 5.5 the velocity at $z = 900$ mm from the ground is displayed, the section plane is just above the mirrors. The disturb caused to the flow by them is noticeable, with their wake extending beyond the trunk of the car. Moreover, the flow accelerates in proximity of the A pillars and it separates immediately downstream of the C pillars.

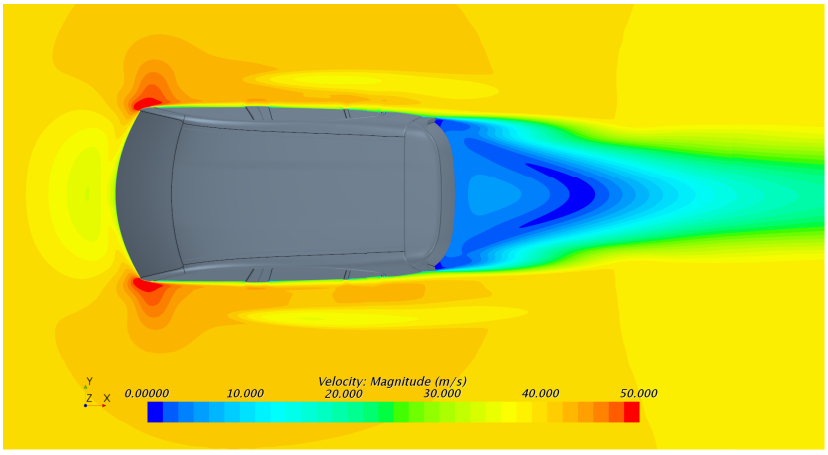

Figure 5.5. Velocity magnitude at $z = 900$ mm.

5.2 Optimisation via surface sensitivity maps

The first optimisation procedure takes advantage of the capabilities of ANSA Pre-processor in translating the surface sensitivity results into a map of nodal displacements. The first adjoint run demonstrates that the spoiler, C pillars and mirrors are the parts with the highest values of surface sensitivity, highlighted in dark blue and dark red in Figure 5.6. For the spoiler, results suggest to reduce its incidence in order to accelerate the flow and

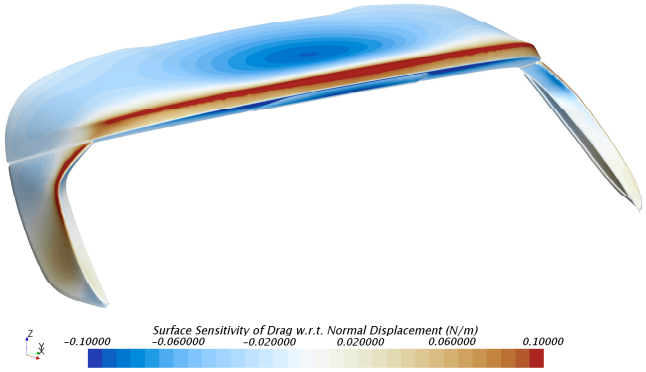

(a) *Spoiler and C pillars.*

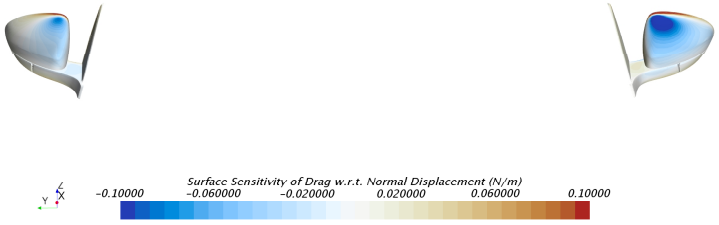

(b) *Mirrors.*

Figure 5.6. Surface Sensitivity w.r.t. Normal Displacement after the first adjoint run.

close the wake. With the same intent the C pillars are pushed inwards. The mirrors are modified to reduce the extension of their wake. Sensitivity of the left and right mirror has different values because they are mounted in an asymmetric manner, therefore the flow around and behind them is slightly different.

For each part, after importing into ANSA the surface sensitivity maps, a maximum displacement has to be specified for every node vectors; they are indicated in Table 5.1. These values are decided as trade-off between an appreciable displacement and good quality of the surface mesh, depending on the modified component. Figure 5.7 shows the outline of the original spoiler and the morphed one.

The verification of the morphed geometry running a new primal simulation confirms

Table 5.1. Maximum displacement for modified parts in ANSA at the first optimisation cycle.

Modified part	**Maximum displacement [mm]**
Spoiler	10
C Pillar	5
Mirrors	3

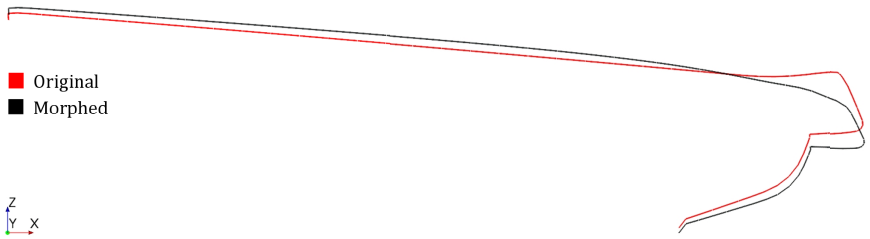

Figure 5.7. Spoiler inclination change after the optimisation with respect to the original configuration.

the correctness of the sensitivity indications. The drag coefficient C_D is reduced by 3.9%. Figure 5.8 shows the pressure coefficient distribution at the rear. Now the suction zone displays higher values with respect to the model in production, especially on the rear window and on the boot door, therefore, as the front end of the car has not experienced any change, the pressure difference between rear and front is reduced, decreasing the pressure drag. It is worthwhile to note also that the overpressure zone on the spoiler trailing edge is no longer evident. Figure 5.9 displays the velocity magnitude in the symmetry plane. The change of the spoiler inclination has reduced the extension in height of the wake, resulting in a minor loss of momentum. An interesting effect of the morphing is provided in Figure 5.10, where the mirror wake at $z = 900$ mm is reduced with respect to the original configuration, especially for the left mirror. Moreover, now the wake closes immediately at the C pillars and the recirculating zone is reduced in length.

In the second optimisation cycle the surface sensitivity suggests to increase the incidence of the spoiler: its intent is to find the right value of the displacement, that is arbitrarily defined by the user. However in this case, as the first shape change has reduced the drag, only the mirrors and the C pillars are modified in the same direction of the previous morphing, following the sensitivity indication. New displacement values are displayed in Table 5.2. Figure 5.11 shows the outline of the car at the left C pillar, providing a comparison with the original shape at different sections in the XY plane.

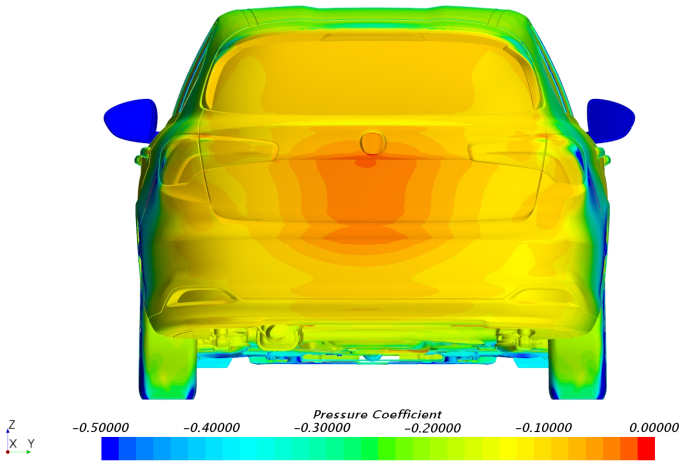

Figure 5.8. Pressure coefficient at the rear of the first modified model.

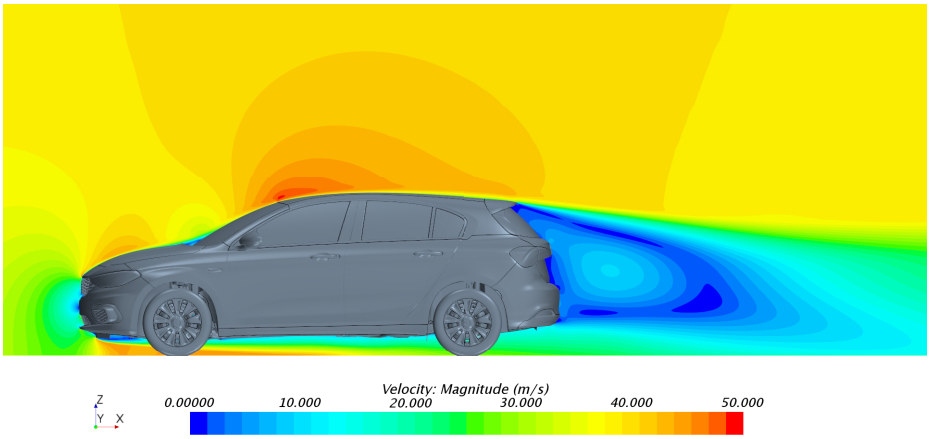

Figure 5.9. Velocity magnitude in the symmetry plane $y = 0$.

Table 5.2. Maximum displacement for modified parts in ANSA at the second optimisation cycle.

Modified part	**Maximum displacement [mm]**
C Pillar	3
Mirrors	3

Once again the morphing has produced a reduction in the C_D value, though only by the 0.3% with respect to the previous configuration. Indeed these modifications are limited on details of the car, therefore we can't expect noticeable improvements. The

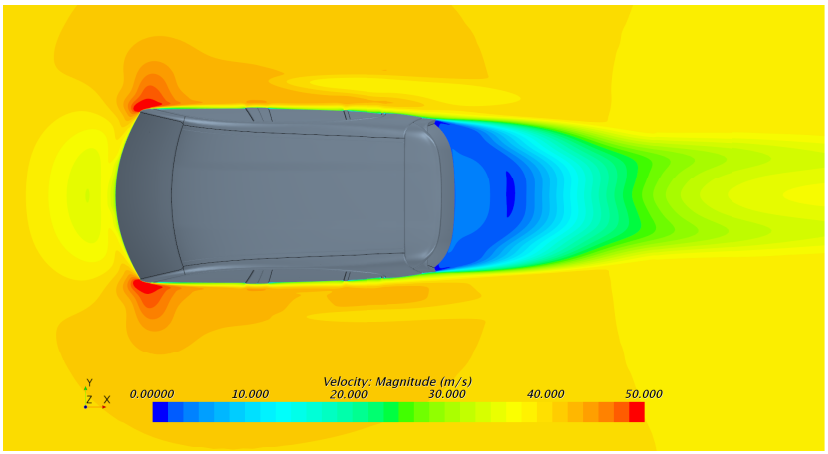

Figure 5.10. Velocity magnitude at $z = 900$ mm.

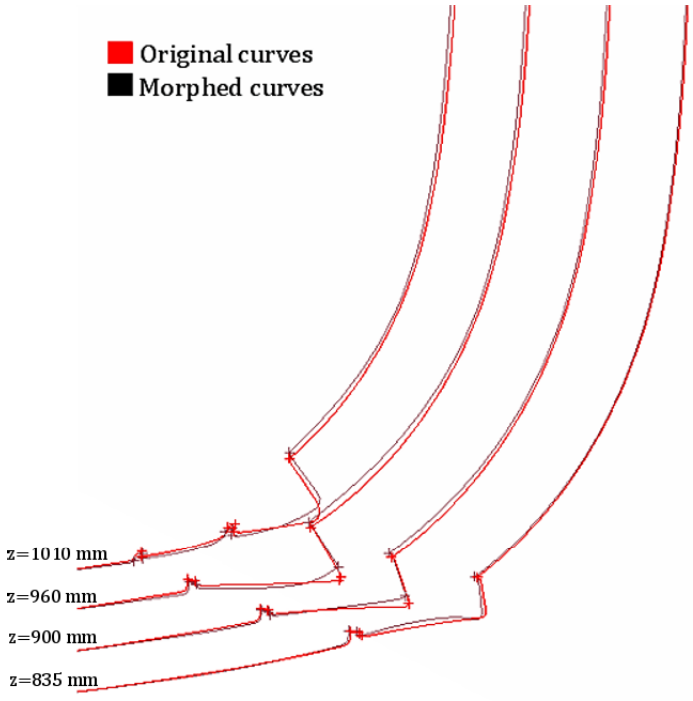

Figure 5.11. Outlines of the C-pillars region at different sections in XY plane.

pressure coefficient distribution displayed in Figure 5.12 doesn't differ too much from the first morphed model, with higher values only on the rear window where the effectiveness of the new C pillars is good. In Figure 5.13 a further improvement of the mirrors wake is clear. At the left side the wake is no longer visible at $z = 900$ mm and at the right side the influence of the mirror is dramatically reduced with respect to the original model.

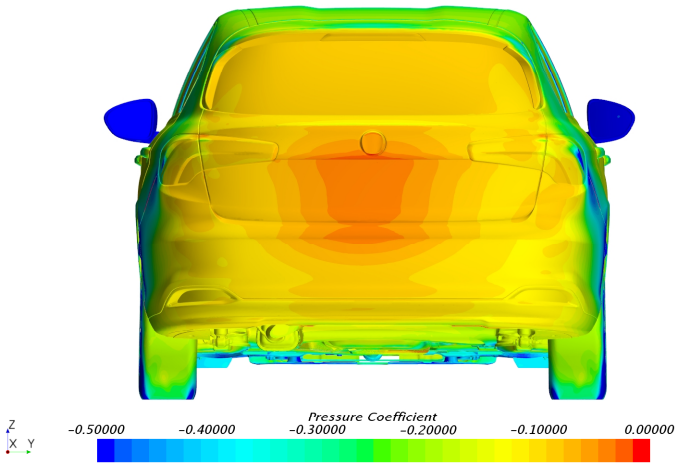

Figure 5.12. Pressure coefficient at the rear of the second modified model.

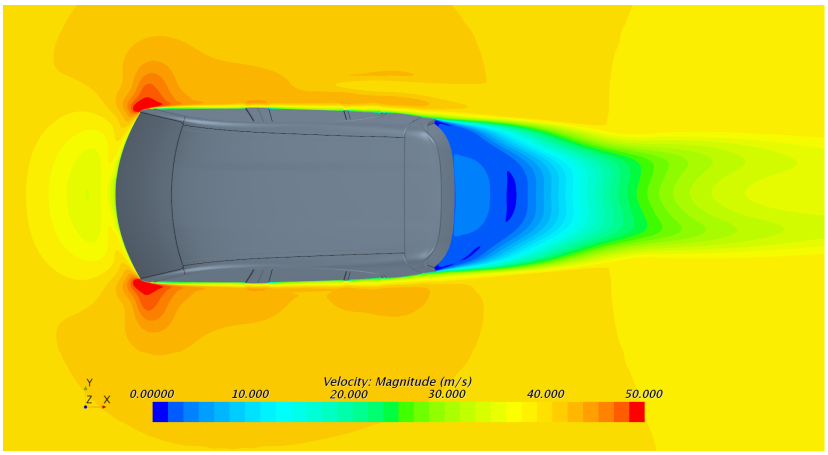

Figure 5.13. Velocity magnitude at $z = 900$ mm.

A clear evidence of the goodness of the modifications is provided by the scene representing the so called *micro drag*, a measurements of the local contribute to the drag in the flow field [16]. It stems from the integral form of the momentum equation. The non-dimensional coefficient is expressed as follows

$$C_{\mu D} = (1 - C_{p_{tot}}) - \left(1 - \frac{V_x}{V_\infty}\right)^2 + \left(\frac{V_y^2 + V_z^2}{V_\infty^2}\right) \tag{5.3}$$

The first term represents the local losses in the flow in terms of total pressure; the second term concerns the local losses in longitudinal velocity and the third term is the drag contribution due to the other components of velocity. The total pressure coefficient is

defined as

$$C_{p_{tot}} = \frac{p_t - p_\infty}{\frac{1}{2}\rho V_\infty^2} \tag{5.4}$$

where p_t is the local total pressure. The micro drag coefficient at the free stream is equal to zero. Figure 5.14 shows at different YZ plane sections the wake generated by the mirrors in the original model and in the last model with a minor extension.

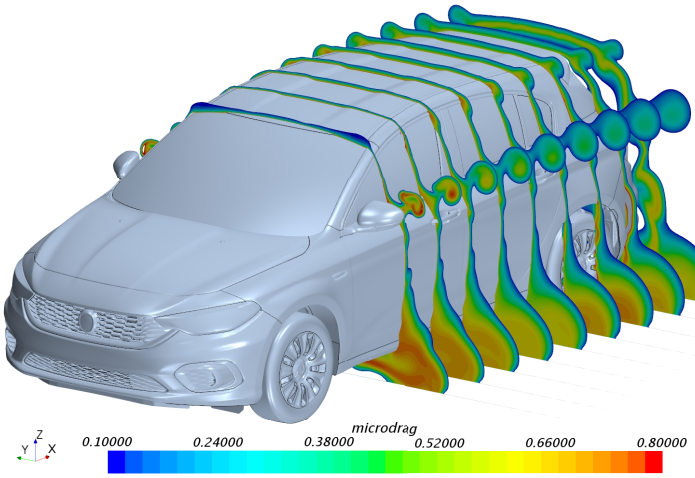

(a) *Original model.*

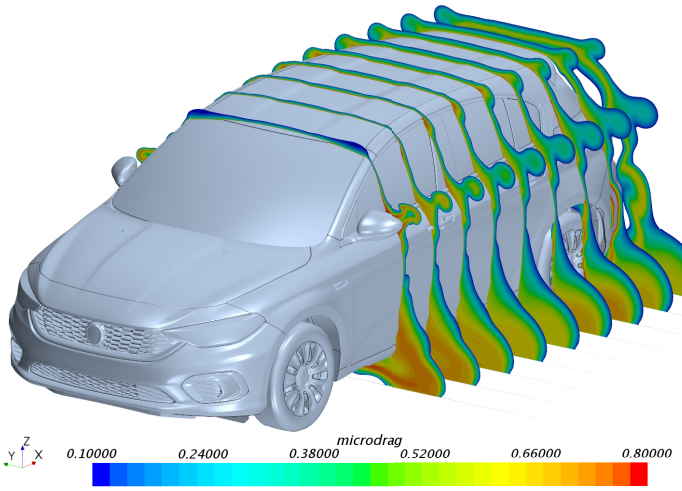

(b) *Second morphed model.*

Figure 5.14. Micro Drag.

In the third cycle the morphing is applied again to mirrors and C pillars, keeping the same values of maximum displacement as shown in Table 5.3. The last primal simulation does not provide appreciable differences in the flow field and the difference in the C_D value

Table 5.3. Maximum displacement for modified parts in ANSA at the third optimisation cycle.

Modified part	**Maximum displacement [mm]**
C Pillar	3
Mirrors	3

remains less than 0.1%, therefore we can consider that convergence is reached.

Table 5.4 summarizes the results of the process in terms of $C_D/C_{D_{ref}}$ and it highlights the delta with respect to the baseline. The overall reduction in drag coefficient is by 4.2%. Figure 5.15 shows the convergence after three optimisation cycles.

Table 5.4. Results in terms of normalized drag coefficient and delta.

Optimisation cycle	$C_D/C_{D_{ref}}$	**Delta**
0	1.000	
1	0.961	-3.9 %
2	0.958	-4.2 %
3	0.958	-4.2 %

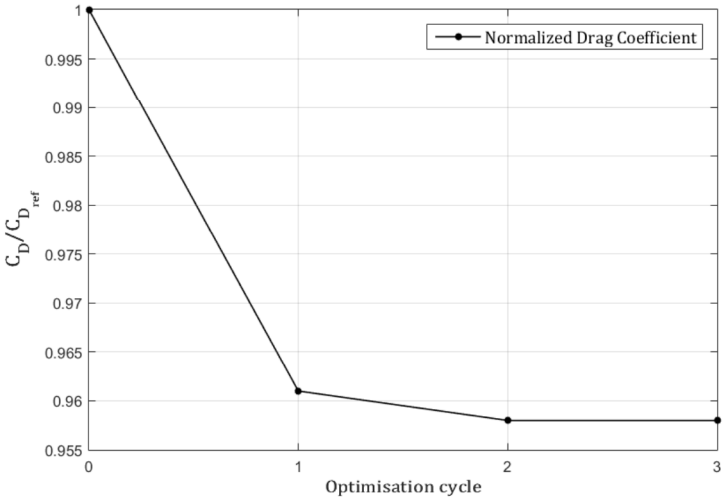

Figure 5.15. Reduction of normalized drag coefficient with morphing in ANSA.

5.3 Optimisation via mesh sensitivity

In this section the results of the process entirely performed within STAR-CCM+ are collected. Starting from the primal simulation with the Standard k-ε model, several steps are performed using the morphing tool available in the software. It uses the results in terms of mesh sensitivity to act directly on the volume mesh and the following primal simulations interpolate the previous results on the new computational grid. As the solver computes the sensitivity on the control points, they have to be insert in a manner as regular as possible in order to avoid asymmetric modifications.

Figure 5.16 shows the cost function gradient with respect to the position of the control points for the spoiler and it has the highest values at the trailing edge, whose inclination has to be reduced. The scale provides the indication to decide the step size in the deformation

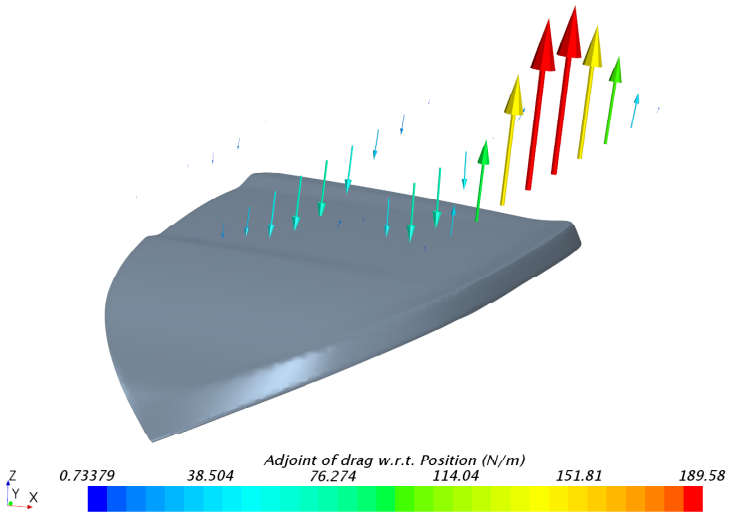

Figure 5.16. Adjoint of Drag w.r.t. Position for the spoiler.

algorithm, it multiplies the gradient computing the nodal displacement. Its value is chosen to perform a change in position in the order of centimetres. Table 5.5 shows the step size associated to the mirrors and the spoiler, the only parts subjected by the morphing in this procedure. The first cycle leads to a lower normalized C_D by 2.9%, obtained again with a new geometry of the mirrors and a reduction of the wake extension, thanks to a different separation of the flow behind the spoiler.

In this case the spoiler is modified also in the following steps in order to reach the optimal configuration, difficult to obtain with one shot. In particular after the second adjoint run the sensitivity suggests again to reduce its inclination at the trailing edge, as displayed in Figure 5.17, hence the previous step size was too conservative. The mesh

Table 5.5. Step size associated to the Adjoint of Drag w.r.t Position at the first optimisation cycle.

Modified part	Step size
Spoiler	$1 \cdot 10^{-4}$
Mirrors	$1 \cdot 10^{-4}$

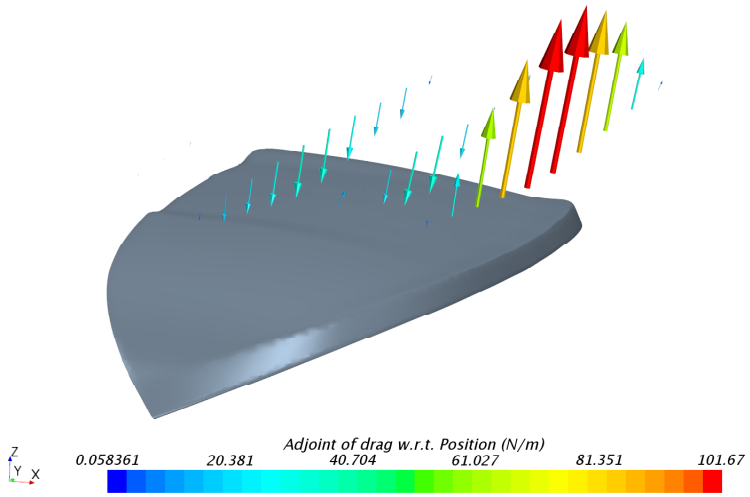

Figure 5.17. Mesh sensitivity after the second adjoint run.

sensitivity has now lower values, the new configuration is closer to the optimum and thus the step size is reduced as shown in Table 5.6. Also the mirrors are morphed in the same sense of the previous cycle in order to reduce their disturb to the flow. After these

Table 5.6. Step size associated to the Adjoint of Drag w.r.t Position at the second optimisation cycle.

Modified part	Step size
Spoiler	$8 \cdot 10^{-5}$
Mirrors	$6 \cdot 10^{-5}$

modifications the normalized drag coefficient is equal to $C_D = 0.964$, with an overall decrease by 3.6%.

Two further optimisation cycles are performed acting on the same parts. The global

reduction in terms of drag is slower than the previous procedure because here the C pillars are not modified for symmetry reasons, therefore the control of the flow separation at the rear relies only on the spoiler. From time to time the surface sensitivity shows lower values, therefore all the modifications can lead to very slight differences in the flow field. Table 5.7 and Table 5.8 display the step size for the third and the fourth optimisation cycle. In the fourth cycle also an attempt to morph the C pillars is done, inserting some

Table 5.7. Step size associated to the Adjoint of Drag w.r.t Position at the third optimisation cycle.

Modified part	**Step size**
Spoiler	$5 \cdot 10^{-4}$
Mirrors	$1 \cdot 10^{-4}$

control points in line, but the values in table show that the sensitivity is not completely symmetric, therefore they are different in order to obtain possibly the same change in shape.

Table 5.8. Step size associated to the Adjoint of Drag w.r.t Position at the fourth optimisation cycle.

Modified part	**Step size**
Spoiler	$2 \cdot 10^{-4}$
Right C Pillar	$1.5 \cdot 10^{-3}$
Left C Pillar	$1.2 \cdot 10^{-3}$

The fifth and last cycle is performed changing slightly only the shape of the spoiler, with the step size equal to $4 \cdot 10^{-5}$. To modify the C pillars in a significant manner many control points have to be inserted with the risk to degrade the volume mesh in the morphing. Even the spoiler would need to find the exact value for the displacement step by step, but it is difficult to manage by hand the decision of a suitable step size every time.

Figure 5.18 and Figure 5.19 show the final configuration of the spoiler and the mirrors respectively with respect to the same parts of the baseline. For the spoiler the reduction of the trailing edge inclination is evident, but the surface is quite flat in the initial part, moreover the new shape is different with respect to the optimised shape of the previous section. In fact it is worthwhile to remember that STAR-CCM+ and ANSA deform the

mesh according to different functions, mesh sensitivity and surface sensitivity respectively, therefore though both methodologies drive to a decrease of the cost function, the results in terms of morphing and thus in the resultant flow field are slightly different.

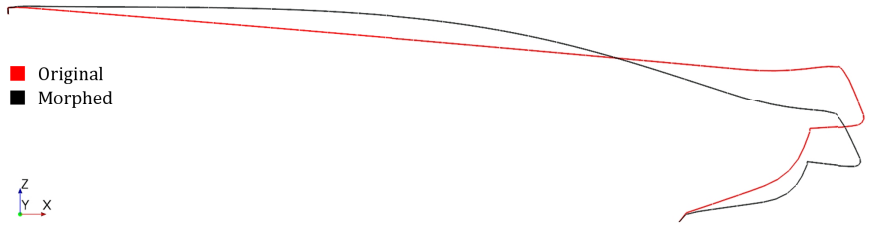

Figure 5.18. Spoiler inclination change after the final step with respect to the original configuration.

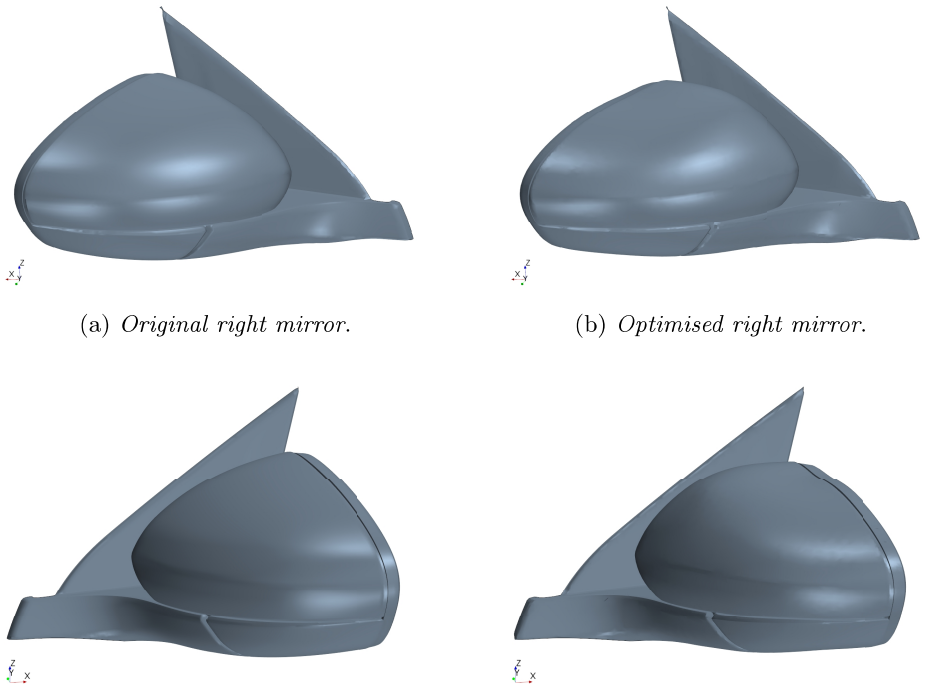

(a) *Original right mirror.* (b) *Optimised right mirror.*

(c) *Original left mirror.* (d) *Optimised left mirror.*

Figure 5.19. Mirrors.

Figure 5.20 shows the absolute magnitude of the cumulative morpher displacement, i.e. the total movement of every mesh node after the complete optimisation cycle, for the spoiler, C pillars and mirrors. The trailing edge of the spoiler, that displayed the highest values of sensitivity, has experienced the major deformation, less than 2 cm.

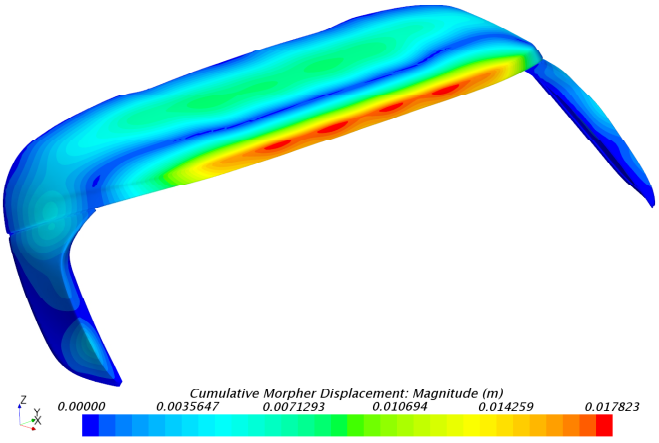

(a) *Spoiler and C pillars.*

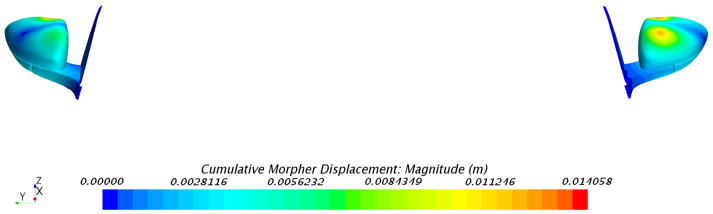

(b) *Mirrors.*

Figure 5.20. Cumulative morpher displacement.

In this part only the aerodynamics of the last morphed model is displayed, as the optimal configuration. Figure 5.21 shows the pressure coefficient distribution at the rear of the last model, recalling the one of the original model for a better comparison. Except for the rear window where there isn't an actual improvement, the suction on the other parts is dramatically reduced, especially on the boot, displaying values closer to zero. It is interesting to note also that the mirrors show a little zone with higher C_p values. The overpressure zone at the trailing edge of the spoiler is reduced.

The wake in the symmetry plane at $y = 0$ is displayed in Figure 5.22. Here the downwash effect provided by the new spoiler can be noted, with a reduction of the wake extension. The wake tends to close downstream, instead in the original model it seems to expand, resulting in a greater loss of momentum, whose balance between upstream and downstream determines the global drag.

Figure 5.23 shows the velocity magnitude at $z = 900$ mm to compare the influence of the mirrors with respect to the primal simulation. Their wake, visible at the beginning, now is completely absent at this section. Also the zone at velocity near to zero at the rear

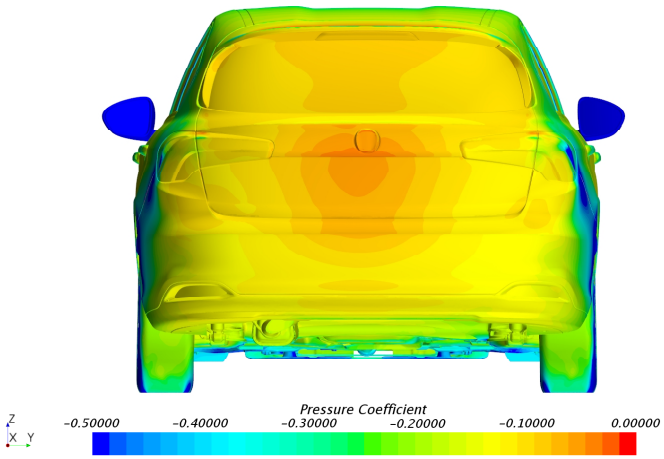

(a) *Original model.*

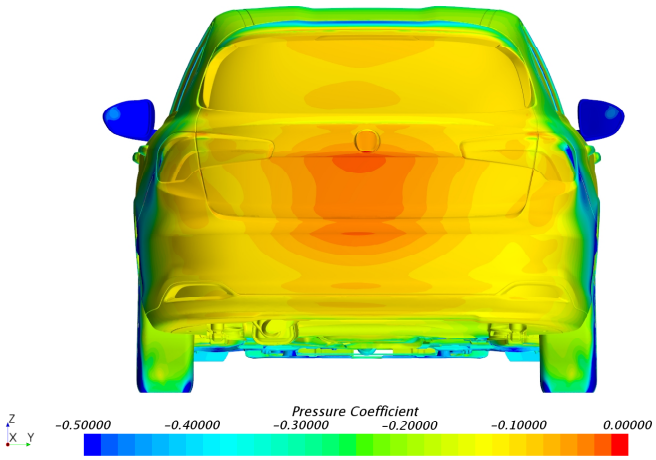

(b) *Optimised model.*

Figure 5.21. Pressure coefficient distribution at the rear.

is considerably reduced.

As in the previous section, the scene representing the micro drag can show the reduced disturb of the mirrors. Not only the core of the wake is smaller, but also the values of micro drag at the plane section in proximity of the mirrors are lower. This features are displayed in Figure 5.24.

In conclusion, Table 5.9 summarizes all the results of these five optimisation cycles in terms of normalized drag coefficient and the overall reduction in percentage of the first coefficient. With different intervention and modifications, the global decrease in drag is the same of that reached morphing the model in ANSA. Figure 5.25 shows the plot of the

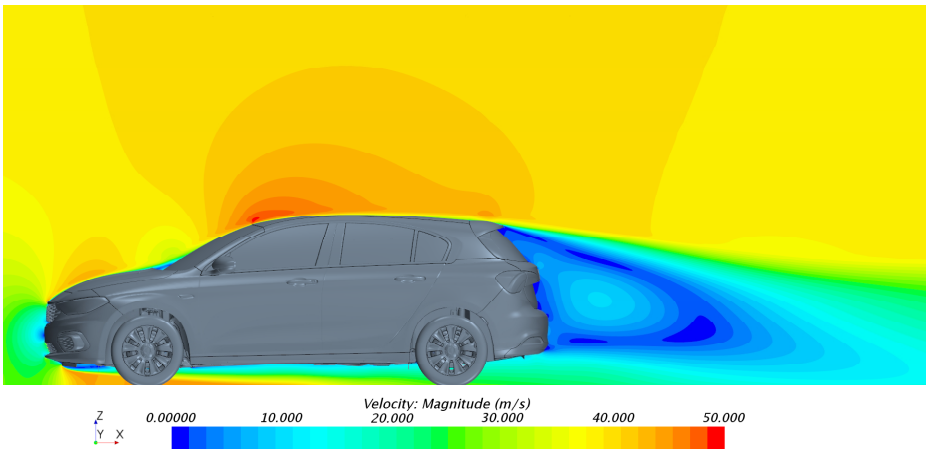

Figure 5.22. Velocity magnitude in the symmetry plane $y = 0$ of the optimised model.

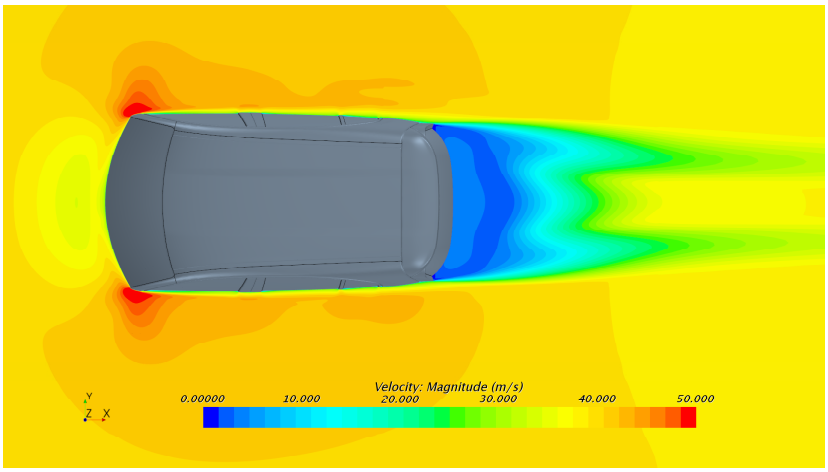

Figure 5.23. Velocity magnitude at $z = 900$ mm.

Table 5.9. Drag coefficient reduction.

Optimisation cycle	$C_D/C_{D_{ref}}$	**Delta**
0	1.000	
1	0.971	-2.9 %
2	0.964	-3.6 %
3	0.961	-3.9 %
4	0.958	-4.2 %
5	0.958	-4.2 %

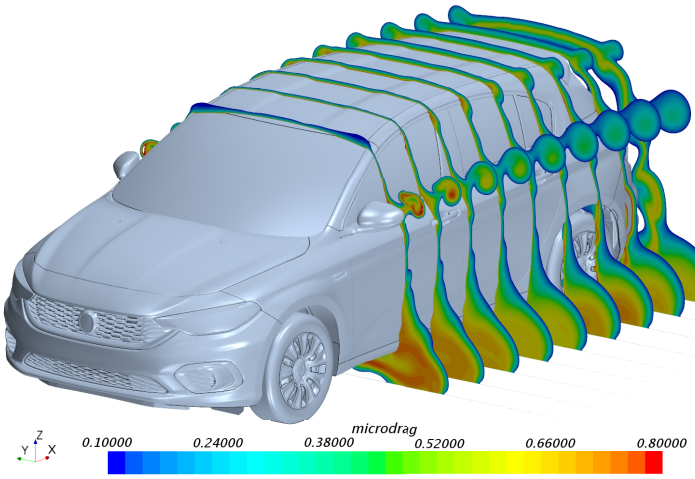

(a) *Original model.*

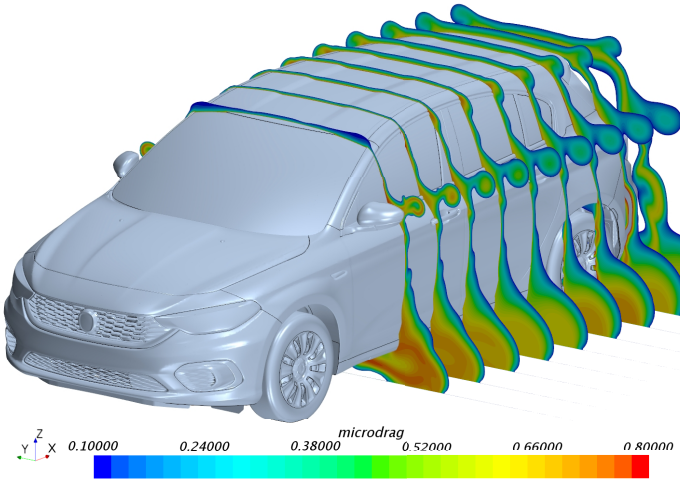

(b) *Optimised model.*

Figure 5.24. Micro Drag.

results.

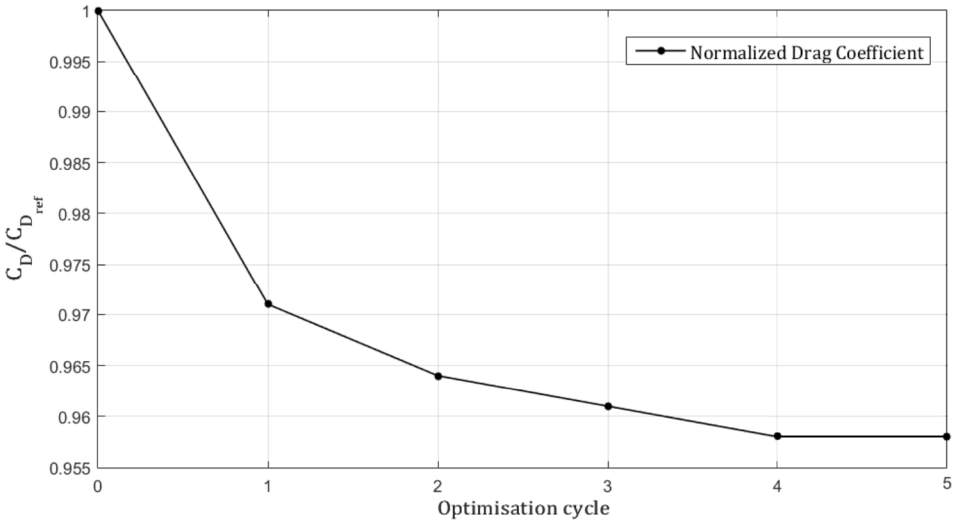

Figure 5.25. Reduction of normalized drag coefficient with morphing in STAR-CCM+.

5.4 k-ω results

Here a brief discussion over a run with the SST k-ω model, using the same mesh of the previous case, is provided. In this case the optimisation process is performed entirely using STAR-CCM+. As this model should be more accurate in resolving the boundary layer, the numerical results of the primal simulation, and even the cost function sensitivities, are slightly different compared to the k-ε solution. Therefore even the starting value of the drag coefficient is different. However, clearly, the flow around the car has globally the same behaviour. Figure 5.26 shows a wide part of the boot with higher values of C_p with respect to the k-ε pressure distribution.

The adjoint run provides the surface and mesh sensitivity, the former is displayed for the spoiler in Figure 5.27. Though the indication is the same provided by the k-ε simulation, the lighter colours of the surface sensitivity scene highlight a minor influence on the drag. Once again the shape changes are applied only to the spoiler and the mirrors with the step size reported in Table 5.10.

Figure 5.28 displays the outline of the spoiler before and after the morphing. Now the variation of the shape is not very accentuate. The cumulative morpher displacement associated to the spoiler and the mirrors in this case represents the global displacement after the single adjoint run. A very slight modification is applied to geometries in this procedure, in fact the reduction of the drag coefficient after the verification is by 1.9%.

In Figure 5.30 is showed the pressure coefficient distribution at the rear of the car

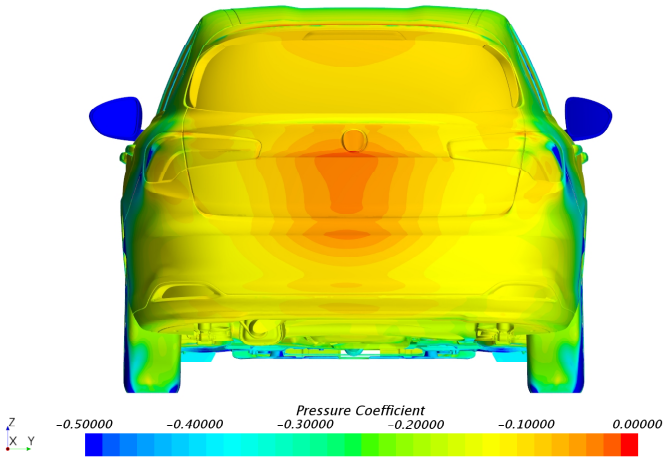

Figure 5.26. Pressure coefficient distribution at the rear.

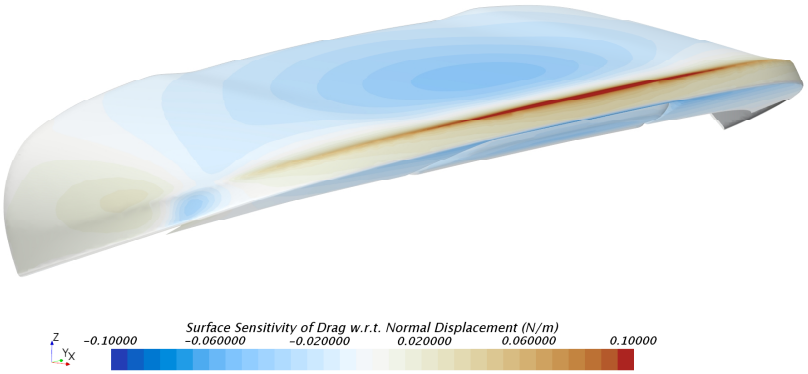

Figure 5.27. Surface sensitivity of drag w.r.t. Normal displacement for the spoiler.

Table 5.10. Step size associated to the Adjoint of Drag w.r.t Position.

Modified part	**Step size**
Spoiler	$1 \cdot 10^{-4}$
Mirrors	$1 \cdot 10^{-4}$

after the morphing phase. The overpressure at the trailing edge of the spoiler is partially reduced but it isn't eliminated as in the previous optimisations. In fact here the spoiler maintains a shape that forces the flow to separate, reducing the downwash effect caused

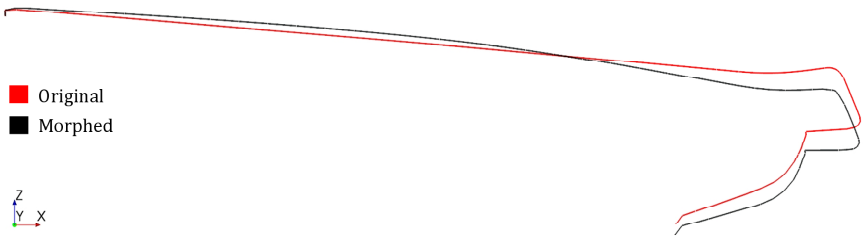

Figure 5.28. Inclination change of the spoiler after an optimisation cycle.

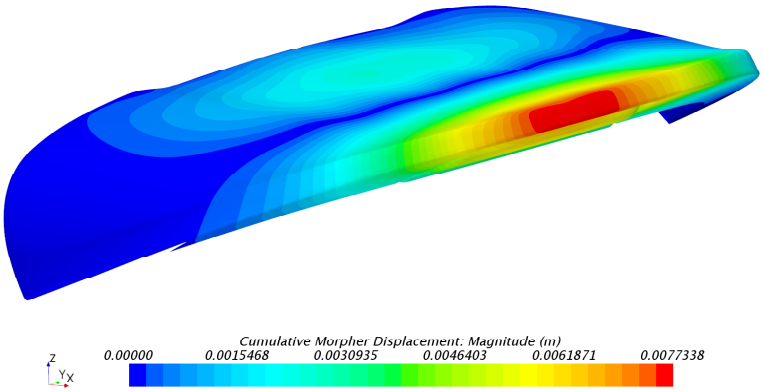

(a) *Surface sensitivity.*

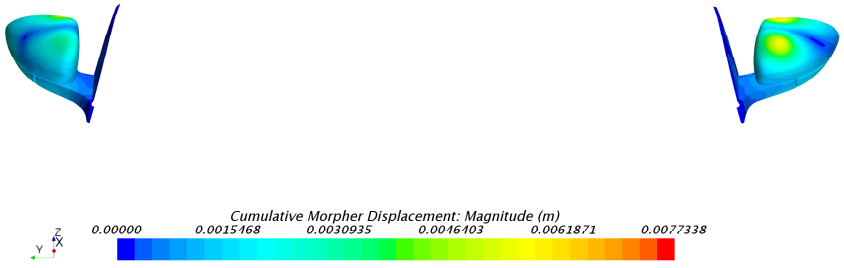

(b) *Mesh sensitivity.*

Figure 5.29. Cumulative Morpher Displacement after the optimisation cycle.

by the considerable change in its inclination. It is also interesting to note that on the rear window, just under the spoiler, the pressure coefficient is reduced, therefore in this part the modification was harmful. However on the boot and on the bumper the suction is remarkably reduced, with a general improvement in the overall pressure difference between the front and the rear end of the vehicle.

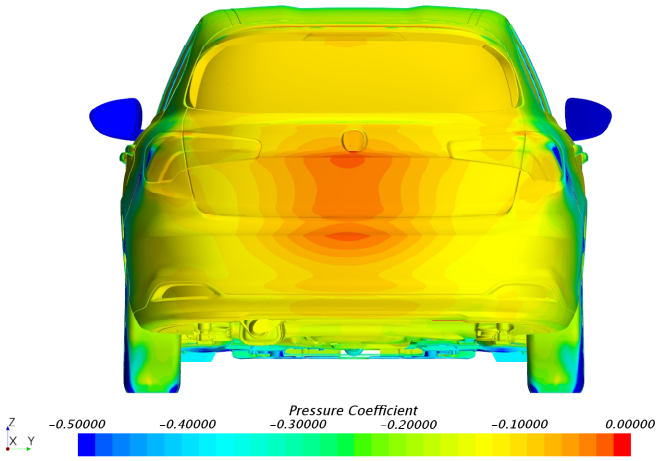

Figure 5.30. Pressure coefficient distribution at the rear of the improved model.

Table 5.11 shows the normalized drag coefficient of the original vehicle and the improved one, respectively. Here the first coefficient is taken as reference, without comparing it to the result of the k-ε primal simulation. Indeed the difference between the two initial drag coefficients relies in the order of magnitude of the deltas that are obtained with the optimisation. It isn't a negligible difference.

Table 5.11. Drag coefficient reduction.

Optimisation cycle	$C_D/C_{D_{ref}}$	**Delta**
0	1.000	
1	0.981	-1.9 %

A unique cycle is performed for this simulation because the k-ω turbulence model has shown a greater sensitivity to the quality of the mesh and going on with the optimisation produces worse results or cells with negative volume. Moreover an adjoint run requires a significant amount of computation time to reach convergence, making this model unsuitable to design purposes.

Chapter 6

Conclusion

In this thesis the potentiality of the adjoint solver of STAR-CCM+ was explored in order to reduce the aerodynamic drag of a passenger car. A practical methodology for reshaping the geometry of the vehicle was researched, in order to verify the possibility to implement it in the design phase. Here the adjoint was applied to an already optimised model, therefore the optimisation process was limited to fine tuning. Probably the adjoint could be more useful in the early design stage, providing a guidance towards the optimal configuration and the improvement of the selected cost function. Implications on other aspects were not considered, like the actual practicability of the morphed shapes. The shape of the mirrors, linked to the dimension of the glass for visibility reasons, is an examples of these neglected aspects.

The attention was focused only on few strategic parts (spoiler, mirrors, C pillars), without changing more complex geometries or less sensitive ones. All the performed changes were often predictable, because they concern the vast experience of the engineers in the design, but this approach was useful in order to verify qualitatively the correctness of the adjoint results. Other parts, like the underbody, were not subjected to the morphing because of failed convergence or difficulty in maintaining a good volume mesh quality after the procedure.

Two different methodologies were followed to find the best one in terms of accuracy and computational time and to manage the optimisation workflow automation. Using the results in terms of surface sensitivity in ANSA has provided morphed geometries with good surface mesh and the global process has reached convergence with only two cycles. The main drawback relies on the use of two software to accomplish the morphing operation and the verification by means of CFD, with the need to remesh the new model when imported into STAR-CCM+. However this methodology is relatively easier to automatise if a default maximum displacement is setted up at the beginning of the process for each

part to morph. The methodology based on the use of STAR-CCM+ to accomplish the entire optimisation has showed a more difficult control of the quality of modified geometry and mesh, depending on the position, the number and the regularity of the inserted control points. Moreover this procedure is difficult to make automatic, because it would be interrupted to visualize every time the results of surface sensitivity to decide where points have to be inserted and the results of mesh sensitivity to create the displacement functions with a suitable step size for each part to morph. In general, it is difficult to establish a priori values of displacement or step size that can be correct for each cycle, because they are subjected to the results of the sensitivities that change every time.

Two different turbulence models were compared to obtain the solution of the primal flow field, the Standard k-ε and the SST k-ω model. The former is largely used in industrial application thanks to its robustness, instead the latter should be more accurate. For this reason the k-ω model would be preferable for an aerodynamics optimisation problem. However it has showed a greater sensitivity to mesh imperfection, making difficult to reach a sufficient convergence for the adjoint solver. Moreover, when convergence is reached, the computational time is considerably larger than the same case running with k-ε model, and this can be a noticeable drawback for the development process. Future works could consider a more deepened study on the k-ω model in order to customize it to accomplish correctly the adjoint simulation, taking advantage of its potential better accuracy.

Another current limitation of this adjoint solver relies on the possibility to be performed only for steady-state simulations with one of the RANS models. For external aerodynamics problems solving the steady-state flow field is a compromise between computational time and accuracy, but indeed the flow around a vehicle have sources of unsteadiness. The car is a typical bluff bodies. For this reason the steadiness is forced using RANS, and probably this could lead to obtain a not completely accurate solution. It would be worthwhile to be able to perform the adjoint using at least URANS, or better a DES, as explained in reference [3].

Bibliography

[1] O. Pironneau. On optimum design in fluid mechanics. *Journal of Fluid Mechanics*, 64:97–110, 1974.

[2] L. Martinelli A. Jameson and N. A. Pierce. Optimum aerodynamic design using the navier-stokes equations. *Theoretical and Computational Fluid Dynamics*, 10:213–237, 1998.

[3] C. Othmer. Adjoint methods for car aerodynamics. *Journal of Mathematics in Industry*, 4:1–23, 2014.

[4] E. M. Papoutsis-Kiachagias G. K. Karpouzas et al. Adjoint optimization for vehicle external aerodynamics. *International Journal of Automotive Engineering*, 7:1–7, 2016.

[5] S. K. Nadarajah and A. Jameson. A comparison of the continuous and discrete adjoint approach to automatic aerodynamic optimization. *AIAA*, Paper 2000-0667:1–9, 1999.

[6] M. B. Giles and N. A. Pierce. An introduction to the adjoint approach to design. *Flow, Turbulence and Combustion*, 65:393–415, 2000.

[7] Stephen B. Pope. *Turbulent Flows.* Cambridge University Press, 2000.

[8] David C. Wilcox. *Turbulce Modeling for CFD.* DCW Industries, 2006.

[9] Jr. John D. Anderson. *Computational Fluid Dynamics: The Basics with Applications.* McGraw-Hill, 1995.

[10] F. R. Menter. *Improved Two-Equation k-ω Turbulence Models for Aerodynamic Flows.* NASA, October 1992.

[11] F. R. Menter. Two-equation eddy-viscosity turbulence models for engineering applications. *AIAA*, 32:1598–1605, 1994.

[12] Siemens. *STAR-CCM+ Documentation: Version 12.04*, 2017.

[13] Dominique Thévenin and Gabor Janiga. *Optimization and Computational Fluid Dynamics.* Springer, 2008.

[14] Joseph Katz. *Automotive Aerodynamics.* Wiley, 2016.

[15] E. Papoutsis-Kiachagias C. Othmer and K. Haliskos. Cfd optimization via sensitivity-based shape morphing. 4^{th} ANSA & μETA International Conference.

[16] A. Cogotti. A strategy for optimum surveys of passenger-car flow fields. *SAE Technical Paper 890374*, 1989.